DESIGN, FABRICATION, AND EXPERIMENTAL CHARACTERIZATION OF A LARGE RANGE XYZ PARALLEL KINEMATIC FLEXURE MECHANISM

by

John Edward Ustick

A thesis submitted in partial fulfillment
of the requirements for the degree of
Master of Science
(Mechanical Engineering)
in The University of Michigan
2012

Advisor: Shorya Awtar, Assistant Professor of Mechanical Engineering

ACKNOWLEDGMENTS

I would like to acknowledge the following persons who helped me grow tremendously throughout my graduate experience, and without whom this thesis would not be complete:

Shorya Awtar, Sc.D., for being far more than a mentor. He is the reason I pursued a Master’s degree, and he has helped me through the ups and downs of graduate school with endless support and advice.

Shiladitya Sen, for teaching me much of what I now know about flexures, as well as providing a significant contribution to the hardware and intellectual content contained within this thesis.

Gaurav Parmar, for providing much needed support in the lab.

Jason Quint and Adrienne Lemberger, for contributing to a large portion of the conceptual hardware design and manufacturing.

The Precision Systems Design Lab, for being a family away from home.

The people in the machine shop, for teaching me the many techniques necessary to produce all of my hardware.

My mom, dad, and sister, for providing endless support.

My friend, Chris Haddad, for helping with numerous revisions.

My fiancée, Leigh Flechsig, for always keeping my outlook positive and encouraging me every step of the way.

TABLE OF CONTENTS

ABSTRACT

A novel parallel kinematic flexure mechanism that provides highly decoupled motions along the three translational directions (X, Y, and Z) and high stiffness along the three rotational directions (Θ_x, Θ_y, and Θ_z) is presented. Geometric decoupling ensures large motion range along each translational direction and enables integration with large-stroke ground-mounted linear actuators or generators, depending on the application. The conceptual design is guided by a constraint map, and qualitatively validated with two physical prototypes. The final proposed design, which is based on a systematic arrangement of multiple rigid stages and parallelogram flexure modules, is analyzed via non-linear finite elements analysis (FEA). The analysis demonstrates an XYZ motion range of 10 *mm* x 10 *mm* x 10 *mm*. Over this motion range, the non-linear FEA predicts cross-axis errors of less than 7.8%, parasitic rotations less than 3.7 *mrad*, lost motion less than 14.4%, actuator isolation better than 1.5%, and no perceptible motion direction stiffness variation. A prototype is fabricated to experimentally validate the predicted large range and decoupled motion capabilities. Experimental measurements demonstrate cross-axis errors of less than 11.6%, parasitic rotations less than 6.98 *mrad*, lost motion less than 17%, actuator isolation better than 1.7%, and no perceptible motion direction stiffness variation. Additionally, the mechanism is integrated into a setup with non-contact sensors and actuators to demonstrate its application in a nanopositioning system.

CHAPTER I

Introduction and Motivation

Flexure mechanisms derive motion from elastic deformation instead of employing traditional sliding or rolling interfaces [1, 2]. This joint-less construction entirely eliminates friction, wear, and backlash, leading to highly repeatable motion. Further benefits include design simplicity, zero maintenance, and potentially infinite life [3].

By virtue of these attributes, flexure mechanisms are widely employed in various design applications, in particular, *multi-axis* flexure mechanisms are used in precision alignment and actuation instruments [39-40], micro-electro-mechanical system (MEMS) sensors and actuators [31-32], energy harvesting devices [17], micro- and nano-manipulators [24], high dexterity medical devices [41], scanning probe systems for precision metrology and nanomanufacturing [42], as well as consumer products [43].

Multi-axis functionality may be achieved either via a serial kinematic [5-6] configuration or a parallel kinematic [7-9] configuration. While a serial kinematic design may be simply constructed by stacking one single-axis system on top of another to achieve the desired degrees of freedom (DoF), such constructions are often bulky, complex, and expensive, due in part to the need for moving cables and for actuators which adversely affect dynamic performance. Parallel kinematic designs, on the other hand, employ ground-mounted actuators and are often compact and simple in construction. Compared to serial kinematic designs, their main drawbacks include smaller motion range, potential for over-constraint, and greater error motions. Conceptually, synthesis of parallel kinematic designs is not intuitive. The key objective is to overcome the above-mentioned traditional drawbacks in the design of an XYZ parallel kinematic flexure mechanism.

The proposed concept is inherently free of geometric over-constraints, resulting in large translational motions along the X, Y, and Z directions, and exhibits small error motions (cross-axis errors and parasitic rotations). Large motion range along multiple axes is critical in many applications, such as nanopositioning and kinetic energy harvesting, which in great part motivated this work.

Nanopositioning systems are macro-scale mechatronic motion systems capable of nanometric precision, accuracy, and resolution [10], and are therefore vital to scanning probe based microscopy, manipulation, and manufacturing [11-12]. Given the lack of friction and backlash, flexure mechanisms are the most common bearing choice for nanopositioning systems. However, most existing flexure-based multi-axis nanopositioning systems are capable of approximately a 100 μm range of motion per axis (see Prior Art section in *Chapter II*). To broaden the impact of scanning probe techniques in nanometrology and nanolithography requires a several fold increase this motion range [13-15]. The challenge here is not only in the creation of a multi-axis flexure mechanism that is capable of large motion range, but also in the mechanical integration of the flexure mechanism with ground-mounted actuators.

Since flexure mechanisms incorporate the motion guidance attributes of mechanisms with the elastic attributes of structures, they are also highly suited for energy harvesting schemes based on a resonant proof mass subject to cyclic inertial loads. Even though the excitation, and therefore the available energy, is generally in multiple directions, most energy harvesting devices employ single axis resonators [16]. Given that the energy harvested is directly proportional to the amplitude of oscillation [17], multi-axis flexure mechanisms with large motion ranges could enhance efficient harvesting of kinetic energy. However, in addition to providing a large range of motion in each direction, any candidate flexure mechanism must also interface with fixed-axis generators for mechanical to electrical energy conversion.

In both nanopositioning and energy harvesting applications, a motion range of several millimeters per axis would be desirable in a macro-size construction. Relevant fields in nanopositioning include scanning probe microscopy [45-48], scanning probe nanolithography [49], and chemical research such as molecular spectroscopy and drug discovery [50]. Energy harvesting applications depend on resonance, with larger ranges suitable for low frequency, high power applications [51].

This thesis covers the conception, analytical evaluation, and hardware validation of an XYZ parallel kinematic flexure mechanism that meets the large-range motion requirement as well as the pertinent actuator/generator integration challenges associated with these applications.

Chapter II lays out the design challenges in addition to providing a brief overview of the existing literature on XYZ flexure mechanisms. *Chapter III* describes the conceptual design process including the design and fabrication of preliminary prototypes. *Chapter IV* provides the details of the final XYZ flexure mechanism design and its motion characteristics, as well as a comprehensive non-linear finite element analysis. The predicted motion performance in terms of motion range, cross-axis error, lost motion, parasitic rotations, and stiffness variation is reported. *Chapter V* presents the experimental validation of the predicted motion characteristics, including the design and fabrication an experimental setup. *Chapter VI* presents an application of the flexure mechanism through the design and fabrication of a nanopositioning setup. *APPENDIX A* discusses additional information regarding the flexure mechanism fabrication procedure. *APPENDIX B* discusses additional information regarding the experimental procedure.

CHAPTER II

Prior Art

The motion axes – X, Y, and Z – must be decoupled from each other so that motion in one axis does not affect or constrain motion in the other axes. Motion range in multi-axis, parallel kinematic mechanisms is often restricted due to over-constraint, typically resulting from a geometric layout that creates coupling between the motion axes. This ultimately leads to binding and restricts mobility.

Moreover, the undesirable *parasitic rotations*, rotations (i.e., θ_x, θ_y, and θ_z) caused by other inputs such as translations, should be inherently restricted and minimized by the kinematics of the design. This eliminates the need for additional actuators, beyond the minimum three needed for X, Y, and Z actuation, to correct these undesired rotations. In addition to providing *geometric decoupling* between the three motion axes, which prevents each motion direction from affecting the other motion directions, it remains important that the flexure mechanism addresses the geometric constraints associated with integrating practically available actuators or generators.

For an XYZ nanopositioning system, linear actuators are a simple solution that prevents the need for any additional transmission. However, most linear actuators [18], including voice coils, linear motors, piezoelectric stacks, and ‘inchworm’ actuators, produce motion along an ‘actuation axis’, defined by their geometry, and do not tolerate off-axis loads or displacements. Thus, in a nanopositioning system, to integrate these actuators with a multi-axis flexure mechanism, the point of actuation on the flexure mechanism must be inherently constrained to move only along the direction of actuation. Furthermore, this point of actuation should neither influence nor be influenced by the actuation in other directions. This attribute is referred to as *actuator isolation* [19].

Similarly, most generators have a fixed linear or rotary axis of motion, defined by their geometry, which is essential for effective mechanical to electrical energy conversion. This geometric requirement has to be accommodated in a parallel kinematic flexure mechanism designed for multi-axis energy harvesting.

Existing systematic and deterministic methods for the design of parallel kinematic flexure mechanisms [20-22] are derived from the study of motion between a ground and a motion stage, and do not address the additional geometric constraints associated with transducers. Hence, existing approaches cannot leverage elastic averaging [23], available with flexure mechanisms, to generate highly symmetric designs. Consequently, most existing parallel kinematic designs rely on qualitative arguments and rationale. Hopkins and Culpepper present a review of many of the current PK design synthesis methods for multiple DoF flexure mechanisms [52]. One common approach is to replace current PK rigid-body mechanism designs with notch flexure in place of the rotational joints. This allows for the use of well-developed techniques, such as screw theory [53-54]. While this aids the synthesis process, most of the resulting designs are very limited in their range. Another approach is a constraint-based synthesis in which constraints are combined to achieve the desired result [20]. While this method allows alternative solutions with larger range, the constraints of intermediate stages are still ignored. A sampling of these designs is presented below.

Several desktop-size parallel kinematic XYZ flexure mechanisms have been reported in the literature, but none provide the desired large-range motion capability (~ 10 *mm* per axis). While some of these designs are true parallel kinematic arrangements, others represent hybrids of a parallel connection between multiple serial kinematic chains.

Davies [7] reports a three-DoF (XYZ) as well as a full six-DoF parallel kinematic design, with a sub-mm range per translational axis. Culpepper and Anderson [24] present a planar monolithic six-DoF compliant structure with a stroke of 100 μm per translational axis. Dagalakis et al. [8] offer a six-DoF hexapod type parallel kinematic design with improved actuator isolation. A six-DoF parallel kinematic stage is reported by Yamakawa et al. [25] that provides a 100 μm range in the X and Y directions, and 10 μm in the Z direction. Yet another XYZ design, with 140 μm range per axis, is presented by Li and Xu [26]. In all these cases, the motion range in each direction is primarily restricted due to inadequate geometric decoupling and/or actuator isolation between the multiple axes.

In the hybrid category, Yao et al. [9] use a parallel connection of three serial kinematic chains, each comprising two four-bar parallelogram flexure mechanisms, to obtain X, Y and

Z motion (85 μm per axis) without any rotation. Arai et al. [27] also presents a spatial arrangement to achieve XYZ motion capability. Actuated by piezoelectric stacks, a motion range of 20 μm is reported. Similarly, Xueyen and Chen [28] employ a 3-PPP parallel mechanism to achieve good geometric decoupling and actuator isolation between the three motion directions. An overall motion range of 1 *mm* per axis is experimentally demonstrated. Another decoupled XYZ flexure mechanism design is conceptually proposed by Hao and Kong [29]. Here each of the three kinematic chains, which are connected in parallel, is individually a serial-parallel hybrid arrangement. While all these designs appropriately address the issues of geometric coupling and actuator isolation, their hybrid serial-parallel construction leads to a relatively bulky and complex construction.

Apart from the macro-scale designs, several multi-axis MEMS designs have been reported for applications in inertial sensing and micro/nano manipulation [30-34]. The performance of these designs is essentially dictated by the fundamentally planar nature of micro-fabrication. Given the small size, these designs generally exhibit a motion range of less than 10 μm per axis. By contrast, this thesis primarily focuses on macro-scale devices and applications where spatial geometries are relevant and beneficial.

CHAPTER III

Conceptual Design

The conceptual design process begins with the synthesis of an ideal flexure mechanism in a given design space and concludes with the proof of concept, consisting of a physical prototype. This chapter will walk through both the conceptualization and physical realization of the XYZ parallel kinematic flexure mechanism.

3.1 Mechanism Synthesis

The mechanism synthesis and conceptualization was first demonstrated in Shorya Awtar's patent for a "Multiple Degrees of Freedom Motion System" [38], and expanded upon in previous works about the XYZ parallel kinematic flexure mechanism [4]. Since there are no direct tools for synthesis of parallel-kinematic flexure mechanisms, a constraint map is used to guide the design process to achieve the desired motion characteristics.

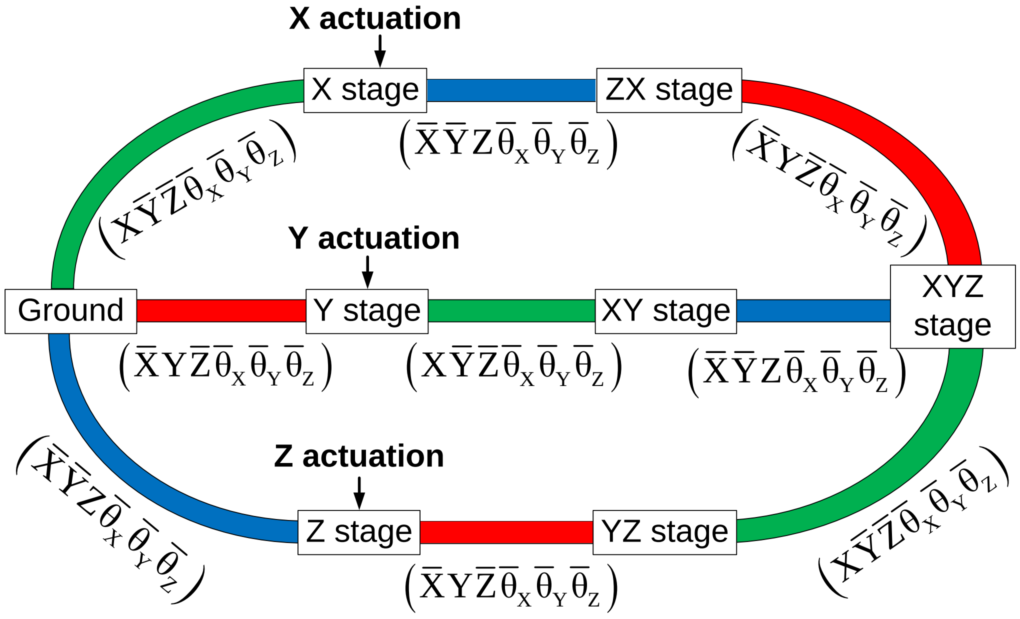

Fig.1 Proposed Constraint Map for Parallel Kinematic XYZ Flexure Mechanism Synthesis

The mechanism must overcome the challenges associated with parallel kinematic design by inherently **(i)** providing geometric decoupling between the X, Y, Z motion axes, **(ii)** constraining motion along the three rotational directions, and **(iii)** providing actuator/generator integration along each translational direction. This constraint map serves as the basis for the synthesis of a novel, compact, parallel-kinematic XYZ flexure mechanism design that embodies the above desired attributes.

The proposed constraint map shown in Fig.1 consists of two elements: blocks for the rigid stages and colored connectors for the constraint elements. The rigid stages are labeled according to the axes along which they are designed to move, i.e. Ground, X stage, Y stage, Z stage, XY stage, YZ stage, ZX stage, and XYZ stage. The constraint elements are classified by color, green, blue, and red, according to the axes along which they guide motion. In addition, the symbols within the parentheses represent the potential three translational and three rotational degrees of freedom (DoF) between any two of the rigid stages. Letters without bars represent DoF directions, and letters with bars represent degree of constraint (DoC) directions. For example, the green elements, denoted by $(X\bar{Y}\bar{Z}\bar{\theta}_X\bar{\theta}_Y\bar{\theta}_Z)$, constrain motion to the X direction only; the red elements, denoted by $(\bar{X}Y\bar{Z}\bar{\theta}_X\bar{\theta}_Y\bar{\theta}_Z)$, constrain motion to the Y direction only; and the blue elements, denoted by $(\bar{X}\bar{Y}Z\bar{\theta}_X\bar{\theta}_Y\bar{\theta}_Z)$, constrain motion to the Z direction only. In the subsequent paragraphs, I describe how such mobility and constraint characteristics are achieved.

For a three DoF parallel-kinematic mechanism, there must be three parallel connecting paths between Ground and the XYZ stage, one each for the X, Y, and Z directions. Each path should have the following characteristics:

i. An actuation stage should be constrained to move in one translational direction only.
ii. Translational motion of this actuation stage should be entirely transmitted to the XYZ Stage, while keeping the XYZ stage free to move in the other two directions.
iii. Rotational motions of the XYZ Stage should be constrained.

Thus, the X stage connects to Ground via a $(X\bar{Y}\bar{Z}\bar{\theta}_X\bar{\theta}_Y\bar{\theta}_Z)$ constraint that allows an X actuator to be integrated at this location. To transmit the resulting X translation of the X stage to the XYZ stage, while permitting relative Y and Z translations, these two stages connect through a $(\bar{X}YZ\bar{\theta}_X\bar{\theta}_Y\bar{\theta}_Z)$ constraint. In other words, the connection between the X and XYZ stages should allow only Y and Z DoF, constraining all others. This is accomplished by connecting a $(\bar{X}Y\bar{Z}\bar{\theta}_X\bar{\theta}_Y\bar{\theta}_Z)$ constraint and a $(\bar{X}\bar{Y}Z\bar{\theta}_X\bar{\theta}_Y\bar{\theta}_Z)$ constraint in series, as shown in Fig.1.

The Y and Z direction actuation paths follow the same rationale to complete the constraint map. This design achieves geometric decoupling by providing actuation in one direction, without affecting the other two directions. The resulting constraint map generates flexure mechanism topologies that provide large, unconstrained translations in the X, Y, and Z directions, as well as actuator isolation between the three translational directions, while restricting all rotations.

To generate a physical flexure mechanism, the constraint map of Fig.1 must be populated with single translational DoF constraint elements. The parallelogram flexure module (PFM), which we have used extensively in the Precision Systems Design Lab for both one and two translational DoF flexure mechanisms, incorporates two or more parallel flexible beams rigidly connected at either end [37, 44]. In this study, I will use the PFM to guide motion along three translational DoF.

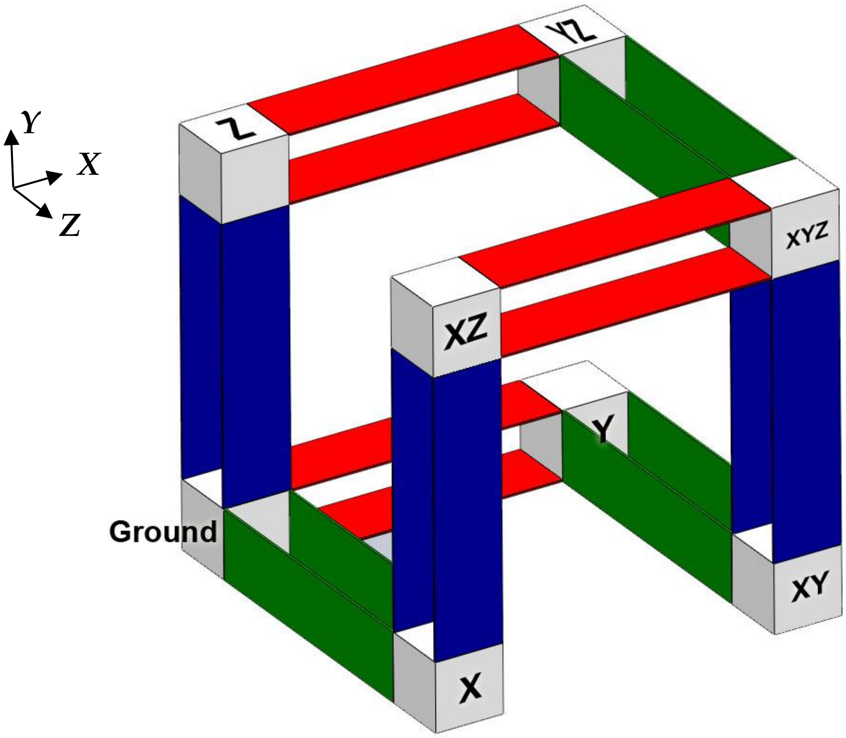

Fig.2 Flexure Mechanism Concept based on Constraint Map

The flexure mechanism produced by populating the above constraint map with PFMs is shown in Fig.2. The white cubes representing the rigid stages are connected by the red, green, and blue PFMs, according to the constraint map in Fig.1. The green PFMs deform primarily in the X direction and remain stiff in all other directions; the red PFMs deform primarily in the Y direction and remain stiff in all other directions; and, the blue PFMs deform primarily in the Z direction and remain stiff in all other directions.

It is important to note that neither the constraint map in Fig.1 nor the physical realization in Fig.2 follow the principles of "exact constraint" design [20]. For example, the rigid stages are over-constrained to reduce potential rotations. This concept may be further augmented by incorporating additional PFMs that serve as non-conflicting constraint elements to produce the highly symmetric, cubic flexure mechanism shown in Fig.3. Again, the enhanced symmetry resulting from this intentional over-constraint of the rigid stages reduces rotations and cross-axis errors, while maintaining geometric decoupling and actuator isolation (See **Error! Reference source not found.**). The distributed compliance of the PFMs enables elastic averaging" [23], resulting in a design that is more tolerant to manufacturing and assembly errors in spite of the over-constraint.

In this parallel kinematic flexure mechanism, the green PFM labeled G1 constrains X stage movement primarily to the X direction, as seen in Fig.3a. Due to their high stiffness in the X direction, the blue and red PFMs transmit the X displacement of this X stage to the XY, XZ, and the XYZ stages. Nonetheless, the XY and XYZ stages remain free to move in the Y direction because of the compliance of the red PFMs, and the XZ and XYZ stages remain free to move in the Z direction because of the compliance of the blue PFMs.

Similarly, the red PFM labeled R1 constrains Y stage movement primarily to the Y direction, as seen in Fig.3b. The green and blue PFMs have high stiffness in the Y direction, thus transmitting the Y displacement of the Y stage to the XY, YZ, and XYZ stages. However, the XY and XYZ stage remain free to move in the X direction because of the compliance of the green PFMs, and the YZ and XYZ stage remain free to move in the Z direction because of the compliance of the blue PFMs.

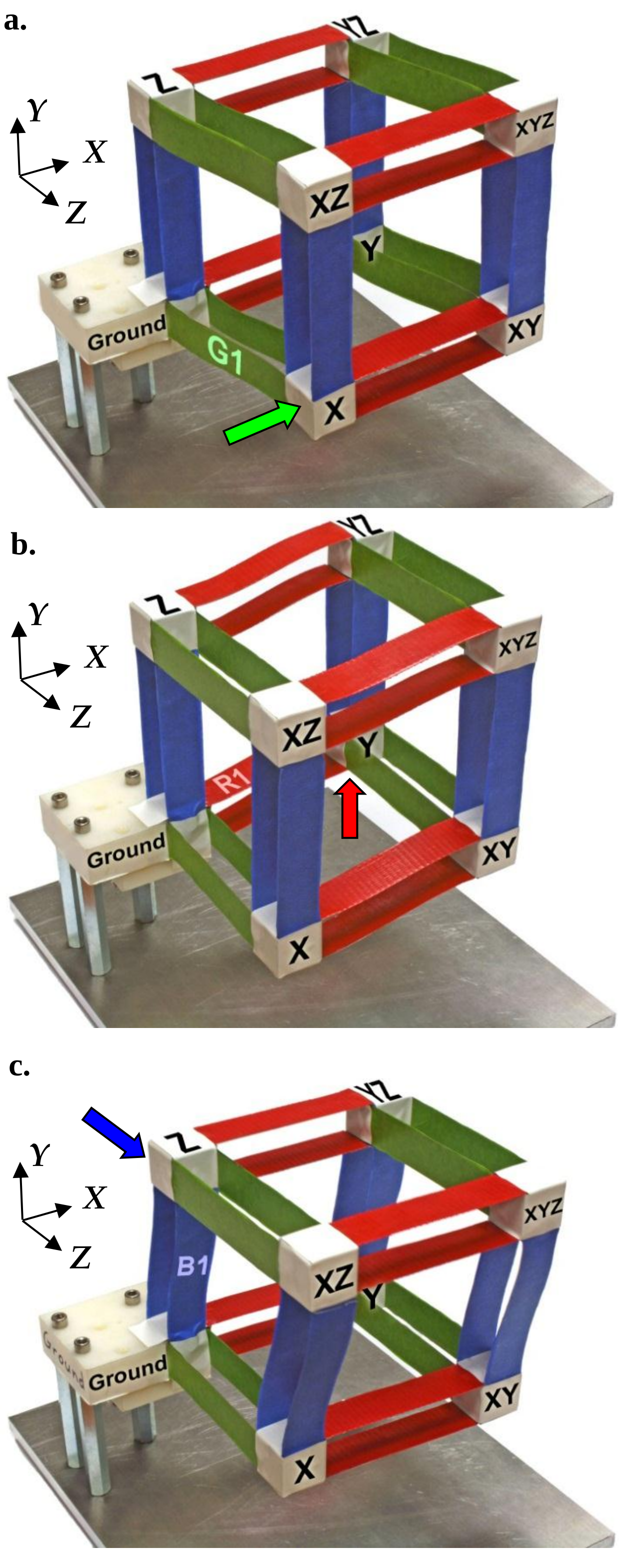

Fig.3 Proposed Flexure Mechanism Design: A. X motion only B. Y motion only, C. Z motion only

Finally, the blue PFM labeled B1 constrains Z stage movement primarily to the Z direction, as seen in Fig.3c. The green and red PFMs have high stiffness in the Z direction, thus transmitting the Z displacement of the Z stage to the YZ, XZ, and XYZ stages. However, the XZ and XYZ stage remain free to move the X direction because of the compliance of the green PFMs, and the YZ and XYZ stage remain free to move in the Y direction because of the compliance of the red PFMs.

In effect, the proposed parallel-kinematic flexure design behaves like a mechanical summation device – the X motion of the X stage, the Y motion of the Y stage, and the Z motion of the Z stage combine to produce the XYZ stage output. In a multi-axis nanopositioning system, the outputs of large-stroke, fixed-axis, linear actuators, mounted at the X, Y, and Z stages, combine to produce motion in three DoF at the XYZ stage.

Conversely, the flexure mechanism also serves as a mechanical separator – the X, Y, and Z motions of the XYZ stage are mechanically separated into an X motion only at the X stage, a Y motion only at the Y stage, and a Z motion only at the Z stage. In the context of multi-axis energy harvesting, large-stroke, fixed-axis, linear generators, mounted at the X, Y, and Z stages, capture energy from a proof mass vibrating in three DoF on the XYZ stage.

The constraint map of Fig.1 can also be populated using other single translational DoF flexure modules, such as the multi-beam parallelogram and the double parallelogram. This would result in different XYZ flexure mechanism embodiments, while containing the same geometric decoupling and actuator isolation behavior as seen above. More detailed motion performance such as error motions, stiffness variations, and dynamic behavior would obviously be different for each. In fact, if the constraint elements were ideal, i.e. zero stiffness and infinite motion in their DoF direction, and infinite stiffness and zero motions in their constrained directions, the resulting XYZ flexure mechanism would also be ideal – zero stiffness in the X, Y, and Z directions, zero parasitic rotations of all the stages, perfect decoupling between the motion axes, perfect actuator isolation, zero lost motion between the point of actuation and the main motion stage.

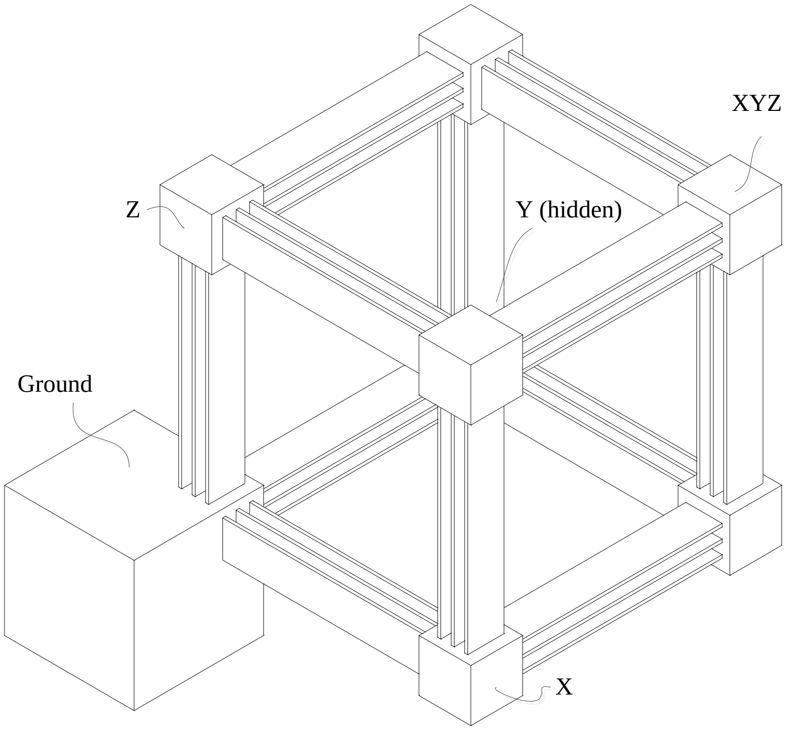

Fig.4 Patent Design of XYZ Flexure Mechanism [38]

However, in reality, elasticity of the flexure material inherently produces small, but finite, stiffness in the DoF direction, and small, but finite, compliance in the constrained directions [36]. This gives rise to small, but finite, deviations from the ideal motion behavior in any XYZ flexure mechanism resulting from the above constraint map.

Therefore, validation of the conceptual design requires a physical model. I designed two prototypes in CAD based on Shorya Awtar's patented design shown in Fig.4 [38], and subsequently fabricated and assembled them for the proof-of-concept.

Unlike planar flexure mechanisms [37], the complex geometry of the XYZ flexure mechanism precludes monolithic fabrication. Therefore, the performance of the device relies heavily on the manufacturing and assembly techniques used. Minimizing the number of unique parts helps to ensure accurate and repeatable fabrication.

3.2 First Prototype

Although the design constraints and manufacturing principles were met, the first design was not adequately analyzed for structural performance. The resulting prototype could flex in its DoF directions, but buckled under its own weight. Therefore, it was inadequate for proving the macro-scale performance characteristics of the concept design. The following presents a detailed design and manufacturing process of the first prototype, and discusses the lessons learned going into the next design.

The proof-of-concept design process consists of three important steps: choosing the material and dimensions of the flexible constraint elements, referred to as beam flexures; conceiving a method of mounting the beam flexures to rigid end plates, creating the PFMs; and determining how to assemble and join all of the PFMs, creating the XYZ flexure mechanism.

As a proof-of-concept, the detailed motion performance characteristics were not as important as the macro-scale validation of the motion range and geometric decoupling between the input axes. Therefore, the primary focus was on mounting and assembling the PFMs, with little emphasis on analyzing bearing performance.

Based on the aforementioned patent design, three-beam parallelograms were chosen as the constraint elements to make use of elastic averaging [23]. Blue-tempered spring steel (ASTM A682, AISI 1095) is chosen for the flexure elements because of its high strength to elastic modulus ratio and its tight tolerance on thickness, resulting in very uniform and predictable motion guidance characteristics [23]. The overall flexure dimensions are chosen to have both a length-to-width ratio and a width-to-thickness ratio on the order of 10:1, which is characteristic for simple beam flexures. With spring steel thickness of 0.011 *in*, the total beam length is 4.00 *in* to allow for the desired motion range of ±5 *mm* based on beam yielding criteria. The beam width and spacing, important for DoC stiffness, are 0.5 *in* and 0.25 *in*, respectively.

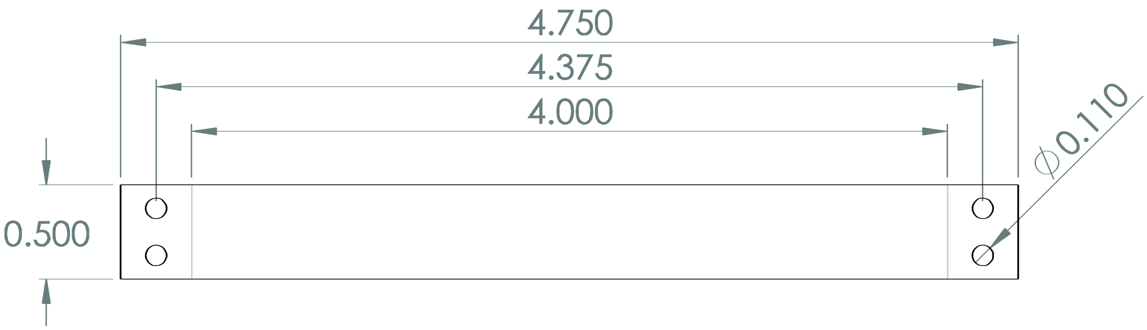

Fig.5 Blue Spring Steel Beam used in First Prototype

The parallel beam flexures are fastened to rigid end plates to create the PFMs, as shown in Fig.6. Important considerations in the assembly include beam alignment, spacing, and end constraint. Beam alignment relies on tight tolerances between beam width and the width of the "U" in the end plates. However, initial testing revealed inaccuracies in the manufacturing processes, resulting in physical binding between the flexures and the rigid end plates. To correct this issue, the "U" was widened, effectively eliminating its contribution to the alignment of the PFMs. The beams are spaced evenly with small blocks made from 0.25 *in* thick Aluminum, with a tolerance that is dependent on the surface finish of the material. Two screws on each side create the constraint by clamping the beams and beam spacers to the rigid end plates. This end constraint design was intended to ensure alignment of the beam ends with the face of the rigid end plate, allowing the PFM to deform in its characteristic "S" shape. However, in practice, the screws did not perfectly constrain the beam ends and spacers. Upon deformation, the screws deflected from their ideal position, leading to misalignment and unexpected mechanism motion.

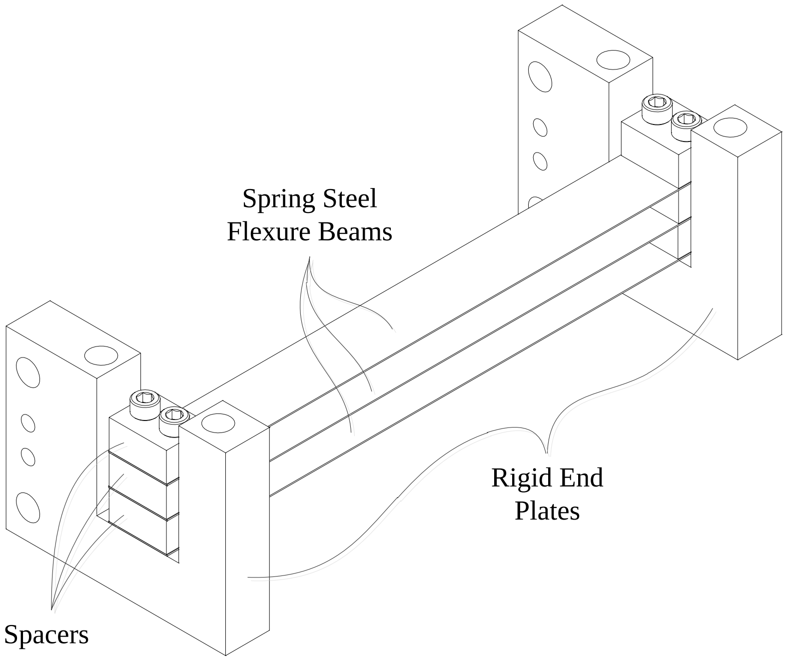

Fig.6 Three-Beam Parallelogram Flexure Module used in First Prototype

The final challenge in creating the XYZ prototype was determining a method of joining and aligning the PFMs perpendicular to each other. The patented concept design shows the beam flexures joining each other at solid cubes in each corner. Based on this concept, the rigid ends of the PFMs come together to form the outside edges of a cube structure. By extending the length of the rigid ends by the amount of their thickness, the “cube” can be assembled with three identical pieces in a symmetric fashion, as shown in Fig.7. Dowel pins pressed through the face of one part into the end of another ensure proper alignment of the PFMs.

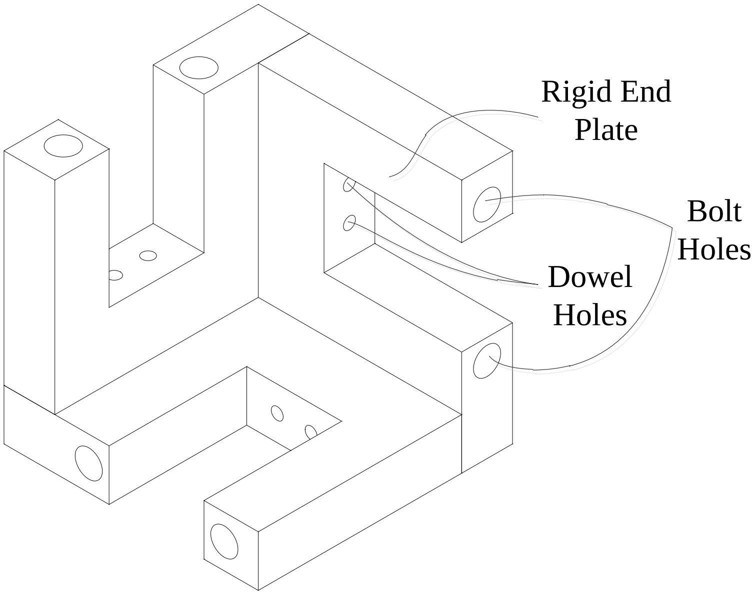

Fig.7 Corner Assembly used in First Prototype

A base is created to mount the flexure mechanism and provide micrometer actuation along the three perpendicular axes. Fig.8 shows the complete XYZ flexure mechanism assembly mounted on a display stand.

Overall, only three unique parts are required to manufacture the flexure mechanism – beam flexures made from 0.008 *in* thick blue spring steel, rigid end plates made from 0.25 *in* thick 6061 Aluminum, and spacers made from 0.25 *in* thick 6061 Aluminum. The spring steel comes in sheets that require cutting to create the desired length and width dimensions. The sheets were cut using a shear; however, the shear produced poor tolerances on length, width, and parallelism, resulting in inconsistency between all of the flexures. Once cut, a custom-made 0.125 *in* diameter punch formed the clearance holes for the mounting bolts. This punch allowed for repeatable positioning of the holes from the ends of the flexures, but the variation in overall beam length meant that the more important tolerance on spacing between the holes from one end to the other was not met. This led to problems in assembly because the maximum spacing between rigid end plates was limited by the shortest flexure, forcing longer elements to be pre-bent during assembly. This ultimately reduced bearing stiffness and lead to unpredictable bearing performance.

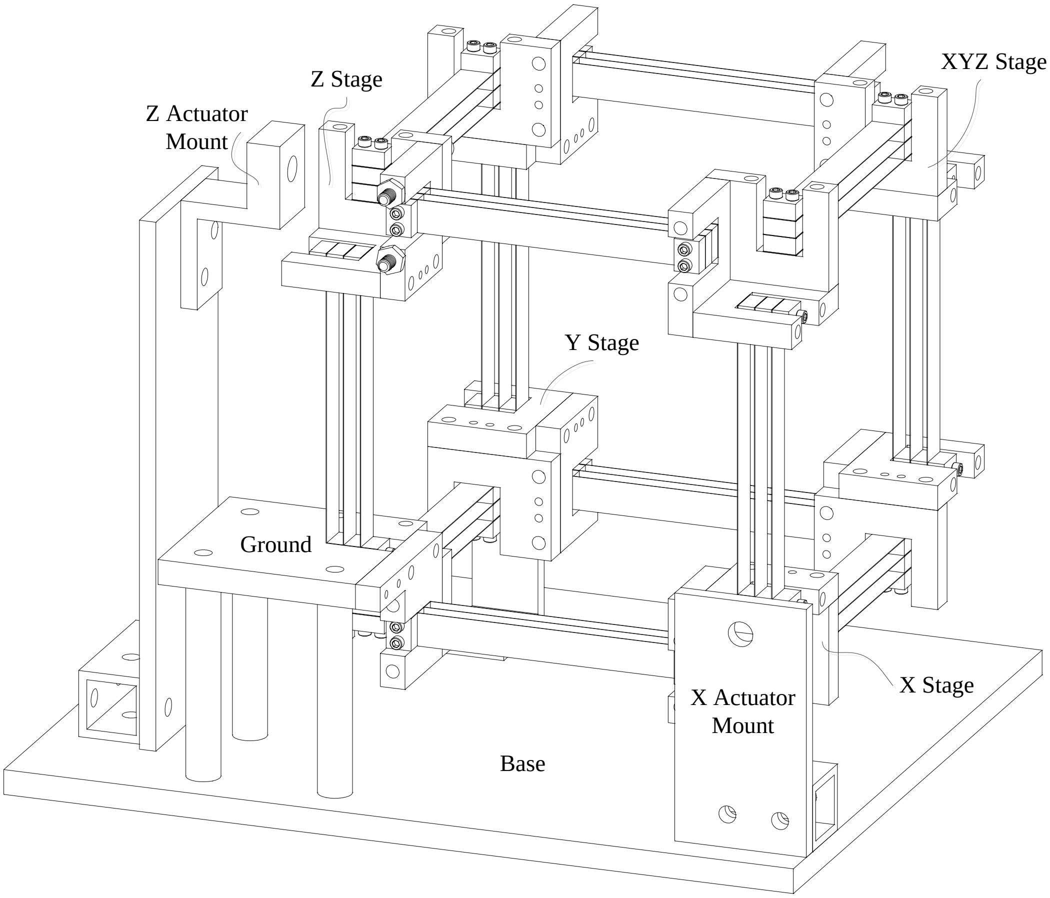

Fig.8 First XYZ Flexure Mechanism Prototype CAD Assembly

Standard techniques were used to fabricate the rigid end plates and spacers. A computer numerical controlled (CNC) water jet cutter quickly created the profiles of the 24 rigid end plates and 72 spacers. Then a mill was used to drill the holes, using a stop to eliminate the need to re-zero between parts.

An alignment tool was used to position the rigid end plates, maximizing the alignment of the flexures within each PFM sub-assembly. The flexures were stacked with spacers and fixed to the end plates with screws. Once complete, the PFM was removed from the alignment tool. The rigid end plates of each PFM were arranged into their respective positions to form the complete flexure mechanism. Each corner assembly was accurately aligned with dowel pins, and then fastened with screws. Finally, the entire mechanism was mounted to the base.

It was immediately obvious that the final assembly could not be used to prove the concept for four main reasons. First, the mass of each rigid corner was too high and the stiffness of the flexures was too low. As shown in Fig.9, the deflection in the vertical direction due to gravity is so large that many of the PFMs are twisting and buckling. This can be resolved by reducing mass, increasing stiffness, or both.

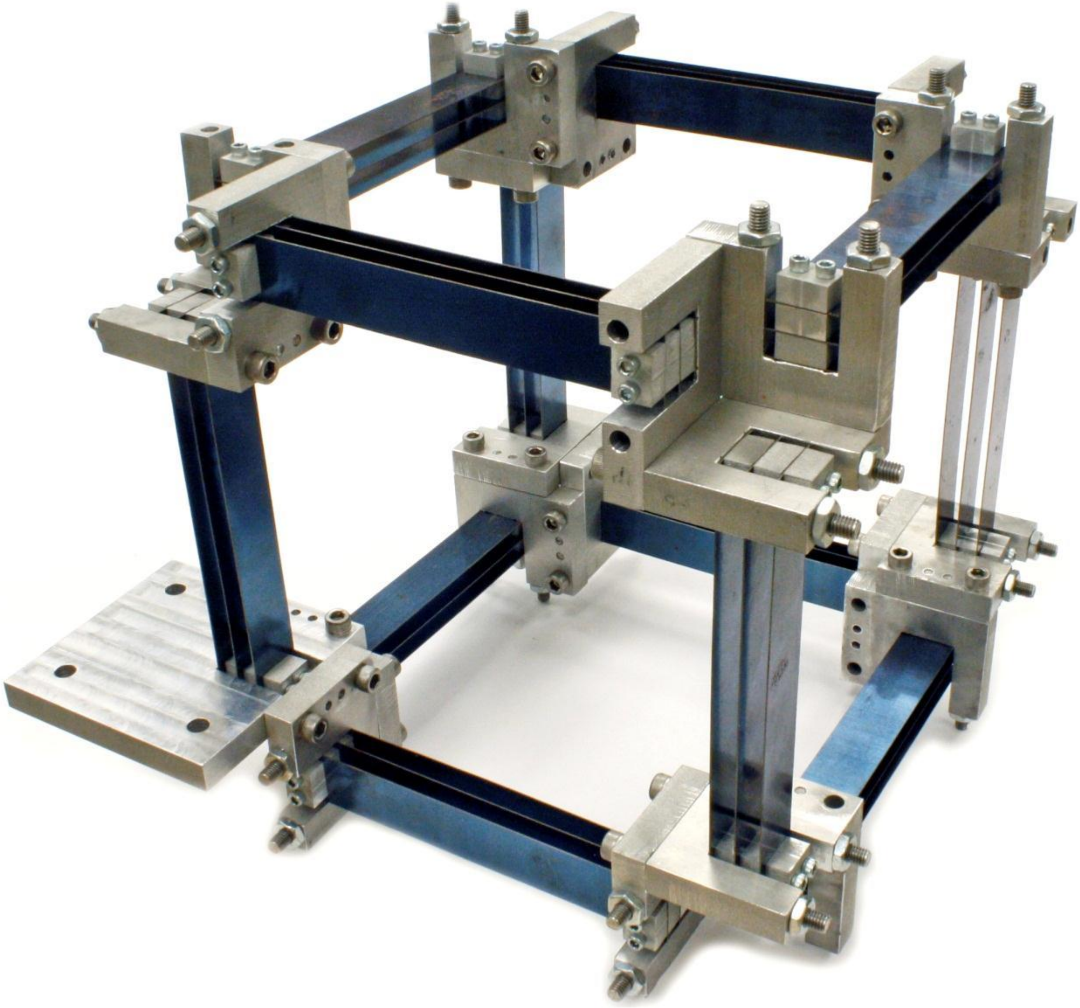

Fig.9 First XYZ Flexure Mechanism Prototype Physical Assembly

Second, the tolerances were not high enough between mating surfaces. While the mass production techniques reduced fabrication time, they also reduced the finish quality to an unacceptable level. The water jet created a rough finish on the edges of the parts with a maximum achievable tolerance of ±0.005 *in*. The alignment of the rigid end plates relative to one another relies on the quality of the mating surfaces, which includes the rough edges created by the water jet. This resulted in a less-than-optimal assembly of the corners. Additionally, the poor surface finish exaggerated the over constraint caused by the dowel pins, making assembly with all of the dowel pins impossible. This can be resolved by finish milling the surfaces with a greater tolerance, and reconsidering the alignment method to eliminate the potential for over constraint.

Third, the dimensional and alignment tolerances of the beam flexures were very low. As noted previously, the shearing process could not produce a consistent final product. The shear tends to lift the material next to the shearing point which causes a variance in width along the length of each piece as much as ±0.05 *in*. This is greater than the intermediate stage “U” width tolerance of ±0.01 *in*. Also, the bolts used to clamp the flexures and spacers were used to constrain the assembly with respect to the stage, but axial forces could bend the bolts slightly. To remedy these problems, the flexures could be cut on the water jet with a length tolerance of ±0.005 *in*, which is an order of magnitude better than on the shear. A better method of constraint is required to ensure proper alignment of the flexures within the PFMs.

Finally, the sheer quantity of parts becomes a large tolerance stack-up. The tolerances of each individual part in series are added, resulting in an unexpectedly large tolerance between the Ground and the XYZ stage. Reducing the total number of parts not only improves the overall tolerance stack-up; it also reduces the number of mating surfaces that require alignment features.

3.3 Second Prototype

The main goal of validating the qualitative performance of the concept design was not accomplished in the first prototype because it buckled under its own weight. Therefore, the next design iteration focused on reducing weight, increasing stiffness, and analyzing the structural performance of the flexures under load to ensure successful completion of the proof-of-concept. To reduce weight, the material used for the rigid ends was changed from Aluminum to plastic. Thicker blue spring steel, 0.011 *in* as opposed to 0.008 *in*, was chosen for the flexures because stiffness increases by thickness cubed. Additionally, I increased beam width from 0.5 *in* to 1.0 *in*, and the spacing between the outermost beams from 0.5 *in* to 1.0 *in*. Increasing these dimensions subsequently increases the rotational stiffness about the axis along the beam's length to help mitigate the buckling seen in the previous design. Preliminary analysis of the effect of gravity on the vertical displacement of the revised bearing predicted only a 0.5 *mm* drop from its undeformed position; a great improvement over the approximately 10 *mm* drop seen on the first design.

Additionally, the method of attaching the flexures to the rigid ends was redesigned to reduce the excess material and total number of components. As mentioned earlier, the constraint map only provides a guide for selecting constraint element types to produce a desired motion. It does not provide any insight into how the components actually come together in the physical world. A design brainstorming session with Prof. Shorya Awtar produced a much simpler concept in which only two beams are used in each PFM, with the rigid ends shared between PFMs at each corner. The result is a single rigid "cube" at each corner that provides alignment and spacing for the ends of three PFMs simultaneously, as shown in Fig.10. The flexures adhere to the plastic cubes with strong glue, and are positioned with an alignment tool. The result is an extremely lightweight and stiff bearing that should be able to support its own weight and demonstrate the predicted performance characteristics.

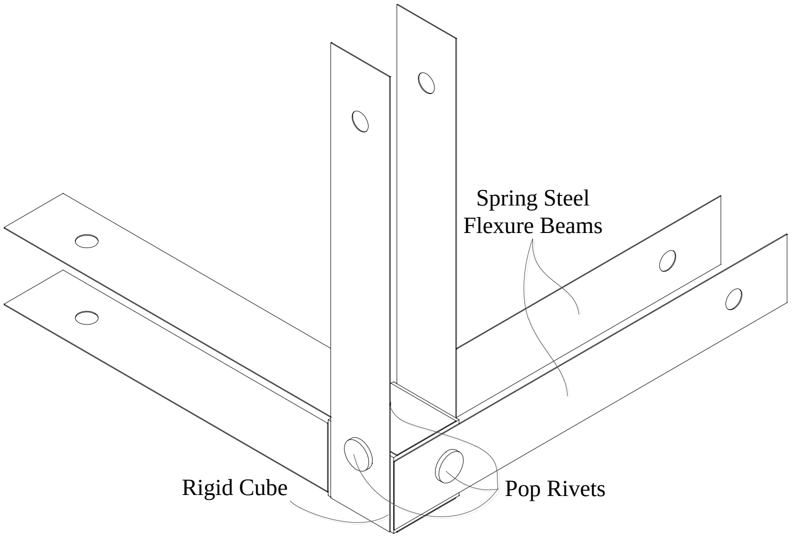

Fig.10 Revised Flexure Attachment for Second Prototype

The much simplified, second prototype has only two unique components – beam flexures made of blue spring steel and rigid cubes made of plastic. The flexures are now cut on the water jet cutter to produce a tolerance of 0.001 *in*, which is an order of magnitude better than those produced using a sheet metal shear. The tolerances are still not adequate for use in a nanopositioner because misalignment, even on the order of 0.001 *in*, can cause greatly varying stiffnesses. However, the tolerances are acceptable for proving the concept. The plastic cubes are cut from a plate, and finish milled to ensure proper dimensioning and flatness. Much slower feed rates must be used when milling or drilling plastic, as heat generated from the cutting process can melt and distort the finish of the material.

During assembly, several different types of glues were tested for adherence and strength. First, ordinary super glue was applied between the spring steel and plastic. Super glue is extremely fast setting, and does not allow sufficient time for proper placement of the flexures with respect to the rigid cube in the alignment tool. Additionally, super glue does not have the peel strength required for the amount of expected bearing deflection. Next, Loctite 1 Minute Epoxy was tried with similar failure. While the setting time is slow enough to allow proper alignment, the peel strength is also inadequate. Finally, a special-ordered industrial strength epoxy, Chemical Concepts K45-S-14ML, which is designed for metal and acrylic, was tested. This epoxy produced very strong fumes, and was difficult to work with because it generated a significant amount of heat. While this last epoxy was the strongest glue tested, it still failed to meet the peel strength requirements. After all testing was completed, it was discovered that the plastic cubes were actually made from Nylon scrap from the lab, which has very poor bonding properties. Materials such as low-density polyethylene or PVC would have provided better adhesive properties, but instead of changing the cube material, a mechanical constraint was added to ensure bonding between the components over repeated cycling of the flexure mechanism.

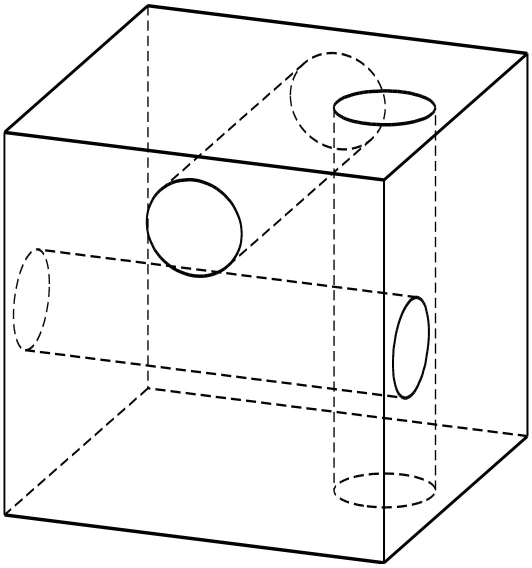

Fig.11 Rigid Cube with Holes for Rivets

The design was modified to include a mechanical constraint element, ensuring a rigid constraint at the ends of each PFM. 1/8 *in* diameter aluminum pop rivets were chosen because they provide a very light weight, yet strong attachment. The cubes were drilled with off-center holes so that three perpendicular rivets could be installed without interference. Fig.11 shows a CAD model of a cube with hidden lines visible to highlight the placement of the holes. Clearance holes were punched on the ends of the flexures to allow for slight manufacturing variation. Even if the cube material had been properly chosen for the glue, a mechanical constraint guarantees a much longer life for the stress cycles imparted through physical interaction with the prototype. The completed flexure mechanism model is shown in Fig.12 below.

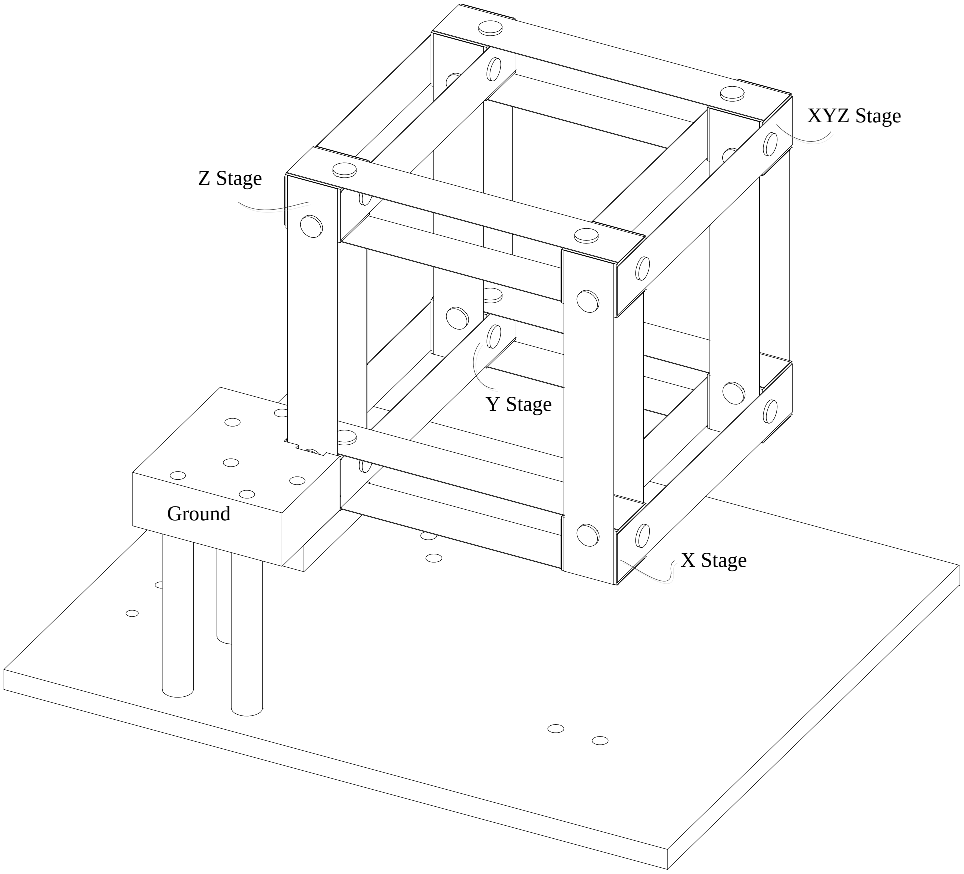

Fig.12 Second XYZ Flexure Mechanism CAD Assembly

The alignment of the bearing assembly with rivets was a two-step process. First, the entire assembly was placed in an alignment tool and glued together. While the glue alone cannot withstand the forces present under loading of the bearing, it is strong enough to hold all of the components together in an aligned position. Next, the rivets can be inserted to greatly increase the rigidity of the bearing under loading. The final assembly, show in Fig.12, is both light and stiff, proving that the concept works as expected. The ability to physically interact with the prototype provided further insight into the motion of the bearing under various loads, and guided my design focus in the detailed design of the final prototype.

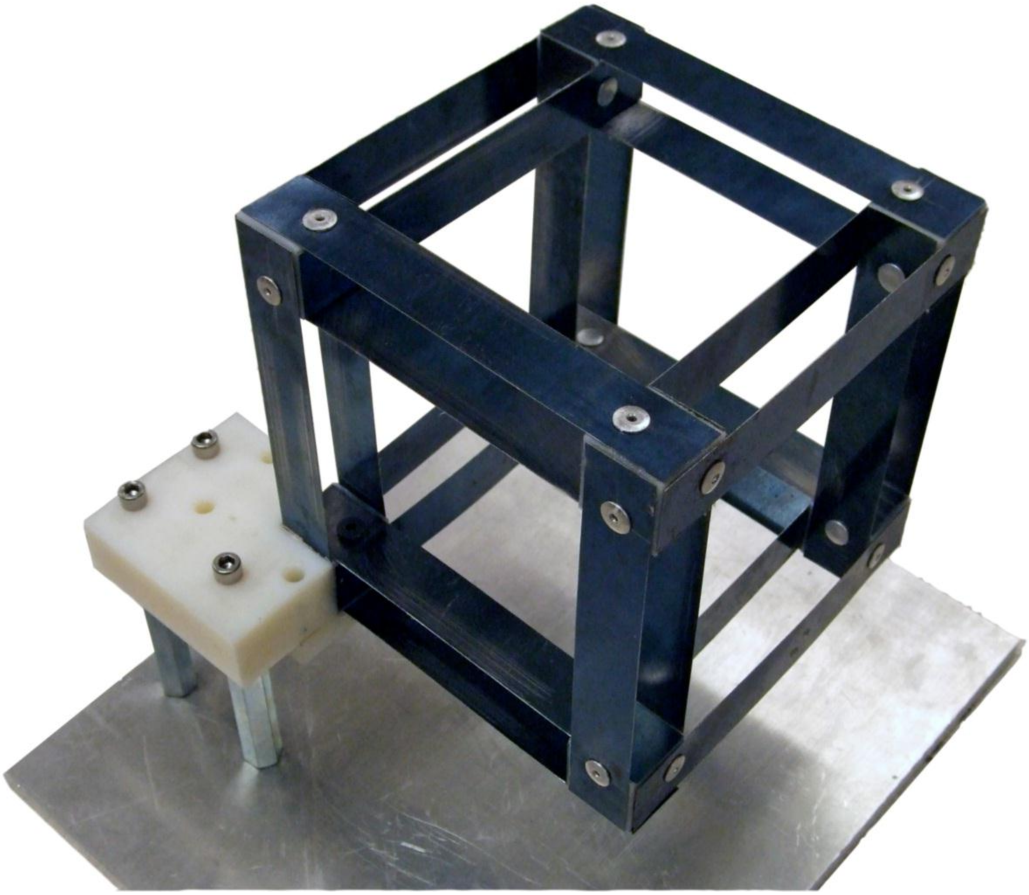

Fig.13 Second XYZ Flexure Mechanism Physical Assembly

While this simple hardware prototype qualitatively validated the expected motion behavior of the XYZ flexure mechanism design, a more detailed prototype is required to quantify deviations from the ideal motion behavior.

CHAPTER IV

Detailed Design

This chapter covers the detailed design of the XYZ parallel kinematic flexure mechanism concept presented in the previous chapter. The design process covers the selection of the flexure material and dimensions based on desired static motion performance and design constraints, prediction of the static motion performance through non-linear FEA, and physical CAD modeling of the entire mechanism assembly for subsequent fabrication and validation.

4.1 Flexure Dimensioning and Material Selection

The overall size, detailed dimensions, and material selection for the flexure mechanism are determined using a static failure (i.e., material yielding) criterion. For a rectangular cantilever beam with a concentrated load at one end, the maximum stress is given by:

$$\sigma = \frac{3 \cdot \Delta \cdot E \cdot T}{2 \cdot L^2}$$

where Δ is the beam end deflection, E is the Young's modulus, T is the beam thickness, and L is the beam length. Given the geometry and constraint pattern of the proposed design, it is evident that the constituent beam flexures deform predominantly in an S-shape. For this deformation, the maximum allowable end-deflection of a beam before the onset of yielding is given by:

$$\Delta \leq \frac{1}{3} \cdot \frac{1}{\eta} \cdot \left(\frac{S_y}{E} \right) \cdot \left(\frac{L^2}{T} \right)$$

where η is the factor of safety, S_y is the yield strength, E is the Young's modulus, T is the beam thickness, and L is the beam length, as shown in Fig.14.

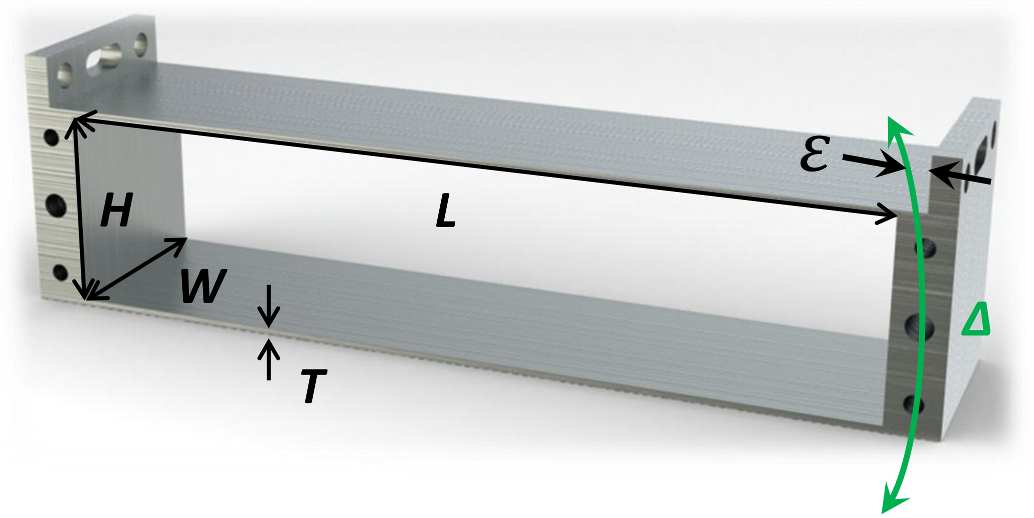

Fig.14 PFM Dimensions

For the material, Aluminum 6061 is selected because of its good flexural properties and machinability. Linear sensors and actuators have a fixed axis of motion, and cannot tolerate much off-axis motion. Therefore, a limit is placed on the maximum expected off-axis motion of the XYZ stage, ε, which is the result of arc-length conservation of the beams:

$$\varepsilon = \frac{3}{5} \cdot \frac{\Delta^2}{L} \leq 150\mu m$$

The desired XYZ stage motion range of 10 mm per direction (or Δ = +/– 5*mm* for individual beams) along with the above two equations dictated the *L* to be as long as possible and *T* to be as small as possible. Furthermore it was found that increasing both beam width, W, and beam separation, H, reduced the rotation of the motion stage. However due to space limitations and manufacturing limitations *L* and *T* are 101.6 *mm* (4 *in*) and 0.762 *mm* (0.030 *in*) respectively, while maintaining a safety factor (η) of 3. CNC wire EDM is the preferred manufacturing process because of its high tolerances and ability to created very uniform, thin-walled sections. However, this process places a limit on the maximum material plate thickness, which corresponds to the beam width. Therefore, the beam width, *W,* is limited to 25.4 *mm* (1 *in*). To maintain cubic corners in the flexure mechanism assembly, the end-to-end beam spacing must also be 25.4 *mm*, resulting in a center-to-center beam spacing, *H*, of 24.64 *mm*.

4.2 Predicted Motion Performance

Predicting the detailed motion performance of large range flexure mechanisms requires a non-linear force-displacement analysis, as shown previously [19, 36]. Ideally, a closed-form, non-linear analysis is preferable since it offers quantitative and parametric insight into the relation between the mechanism's geometry and its motion performance. However, such an analysis entails considerable mathematical complexity and is the subject of our research group's ongoing and future work. Instead, to expediently obtain some early validation and assessment of the proposed design, I conducted non-linear finite elements analysis (FEA) using ANSYS.

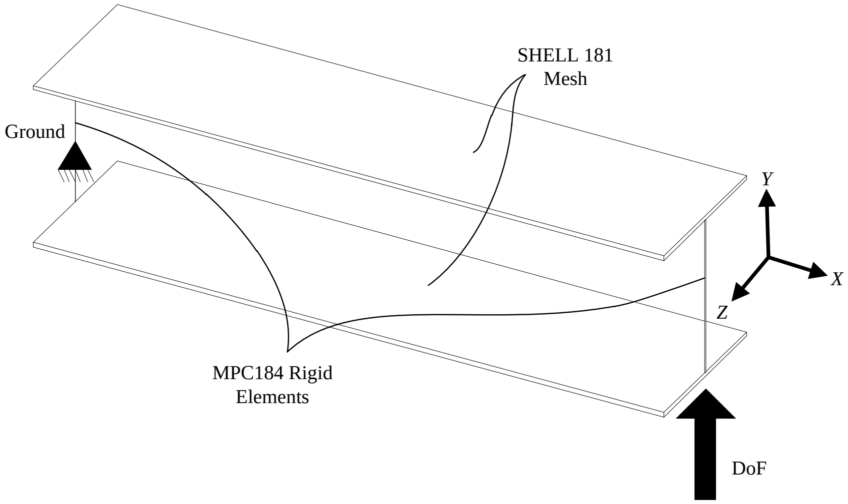

Fig.15 Single PFM Model

Before analyzing the entire flexure mechanism, the stiffness of a single PFM in both the DoF and DoC directions is evaluated. The flexible beams are modeled using a mesh of SHELL181 elements, and the rigid ends are modeled using MPC184 constraint elements. While one end of the PFM is completely constrained, the other end is displaced in the DoF direction, as shown in Fig.15. Forces are applied to calculate translational stiffnesses, and moments are applied to calculate rotational stiffnesses. Throughout this section, *torsional stiffness* refers to the stiffness resisting moments about the X axis of Fig.15, and *shear stiffness* refers to the stiffness resisting forces along the Z axis of Fig.15. The results of the single PFM stiffness analysis help explain the more complex nonlinear behavior of the overall XYZ flexure mechanism shown later.

Fig.16 shows the DoF stiffness over a 10 *mm* range of DoF displacement. The stiffness varies by less than 1% over the entire range. This invariance is expected and, in terms of nanopositioning, it is desired because it allows for the use of linear feedback controls.

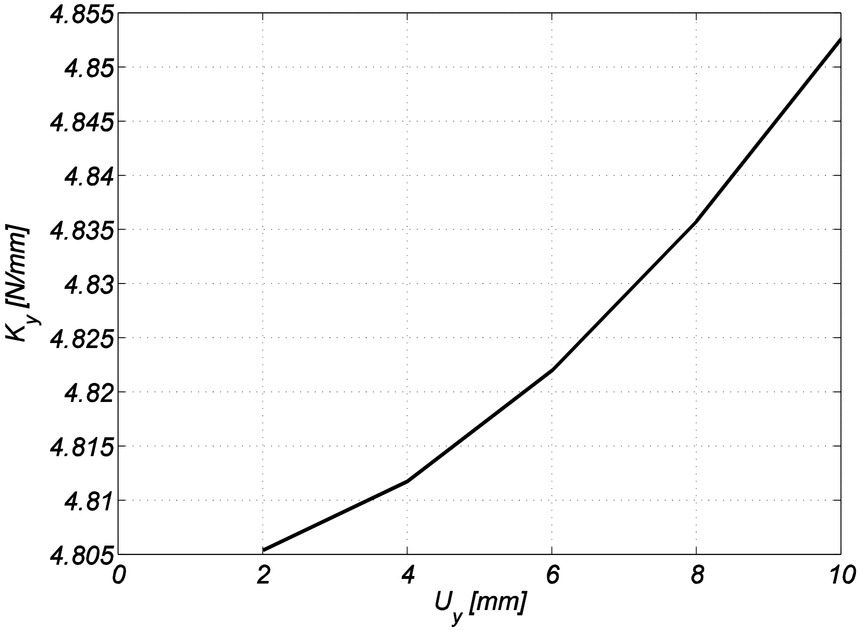

Fig.16 Single PFM DoF Stiffness (UY)

Fig.17 shows the translational DoC stiffness in the Z direction over a 10 *mm* range of DoF displacement. This stiffness is 250 times greater than the DoF stiffness when the DoF displacement is near zero. However, the shear DoC stiffness drops with DoF displacement by 52% at 10 *mm*.

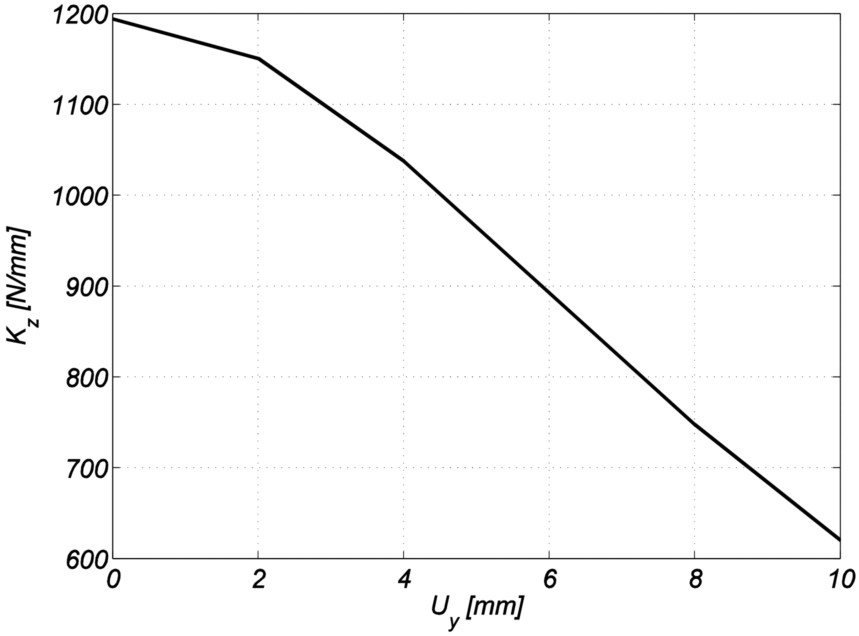

Fig.17 Single PFM DoC Stiffness (UZ)

Fig.18 shows all three rotational DoC stiffnesses over a 10 *mm* range of DoF displacement. The stiffness of the rotational constraint about the Z axis, denoted $K_{\Theta z}$, is the largest. The stiffness of the rotational constraint about the Y axis, denoted $K_{\Theta y}$, is only 33% as large as $K_{\Theta z}$, while the stiffness of the rotational constraint about the X axis, denoted $K_{\Theta x}$, is only 5% as large as $K_{\Theta z}$. Additionally, all three stiffnesses drop with DoF displacement. Under loading conditions where an off-center force causes a moment, the low $K_{\Theta x}$ stiffness results in undesired rotations of the PFMs in the flexure mechanism.

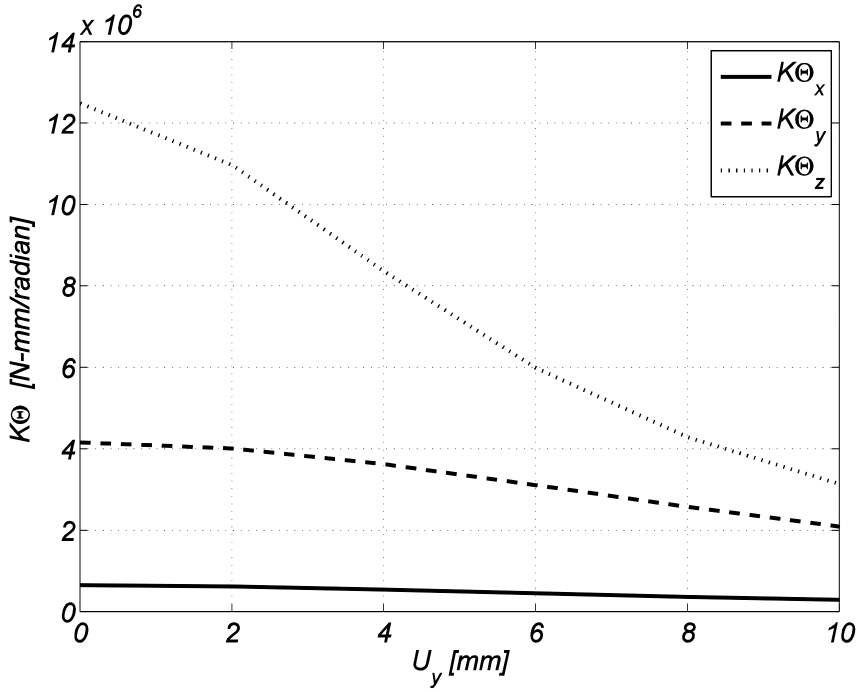

Fig.18 Single PFM Rotational DoC Stiffness

Next, the entire flexure mechanism is analyzed using FEA. The beams are modeled using SHELL181 elements, and the corner stages are modeled using the MPC184 rigid elements. The mesh density was tested and optimized for speed and precision of analysis to be a 64 by 16 mesh of square-shaped shell elements along each beam. To capture the pertinent nonlinearities, the large displacement option (NLGEOM) is turned on. Standard material properties for Aluminum 6061 are assumed (E = 68,900 $N.mm^{-2}$ and ν=0.33). The displacement in each direction are varied over a range of –5 *mm* to +5 *mm* in 5 equal increments, resulting in a total of 125 loading conditions that are analyzed. While reporting the FEA results in the following paragraphs and figures, we follow a nomenclature in which the super-script represents the rigid stage being considered and the sub-script represents the relevant direction of displacement, rotation, or force associated with this stage. For example, U_x^Y represents the X direction displacement of the Y stage, θ_y^Z represents the Y direction rotation of the Z stage, F_z^X represents the Z direction force on the X stage, and so on.

The FEA revealed several unexpected trends resulting from the application of actuation forces away from the mechanism's center of stiffness. The *center of stiffness* (CoS) is defined as the point on each plane perpendicular to the actuation axes at which an actuation force applied through the actuation stage produces minimal rotations at the XYZ stage. Actuating through the CoS is critical for bearing performance because parasitic rotations cannot be actively controlled by the three linear actuators. The exact CoS for each actuation stage is difficult to determine, and does not remain constant for all combinations of X, Y, and Z actuations. However, an estimate of the CoS for each actuation direction can be determined through minimizing the XYZ stage rotations in a static displacement FEA of the mechanism.

Fig.19 illustrates the approximate location of the center of stiffness on the YZ plane for an actuation force applied along the X axis, represented by the circle. Applying a force at the X stage along the X axis, as shown in Fig.19 a., produces parasitic rotations at the XYZ stage because the force is not applied through the CoS. The force applied in Fig.19 a. can be alternatively represented by an equivalent force applied to the X stage from the CoS and moment about the Y and Z axes, represented by the small red and blue double arrows, respectively, as shown in Fig.19 b. These moments are resisted by torsional stiffness of the mechanism; however, the constraints are not ideal and result in small, but finite, rotations. The effect of these rotations is discussed in greater detail below.

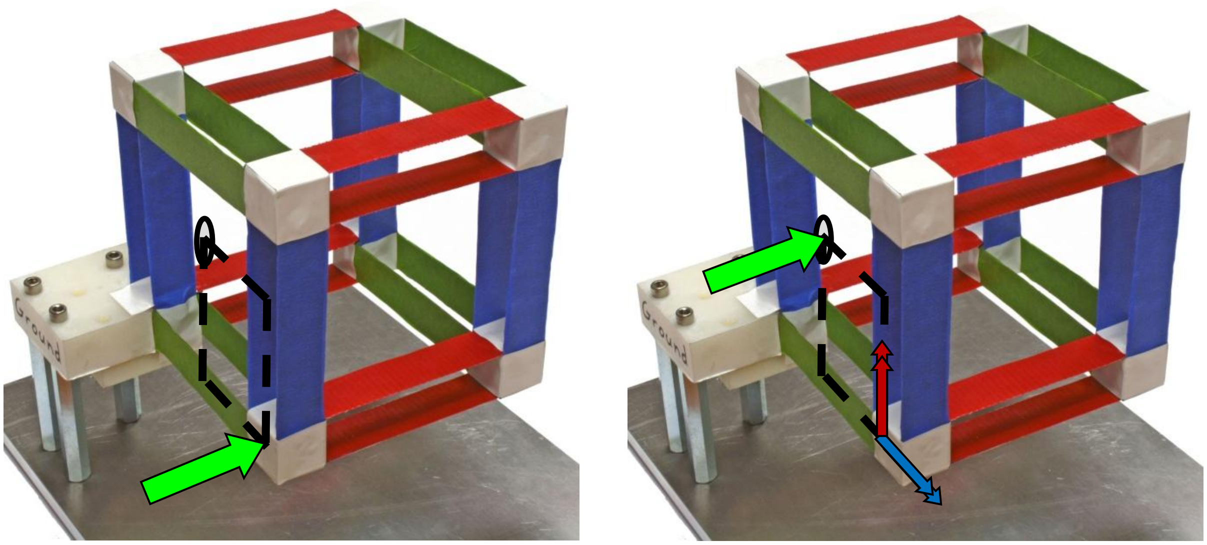

a. Force applied away from CoS

b. Equivalent force at CoS and moments

Fig.19 Moments Caused By Off-Center Force Application

I now present the FEA results for the entire XYZ flexure mechanism. Fig.20 illustrates the geometric decoupling between the X, Y, and Z motion directions in the proposed design. The X direction force applied at the X stage (F_x^X) is plotted versus the X direction displacement of the X stage (U_x^X), for various combinations of Y and Z actuation (U_y^Y and U_z^Z). The resulting X direction stiffness not only remains constant over the entire X direction motion range, it is also largely insensitive to actuation in the Y and Z directions.

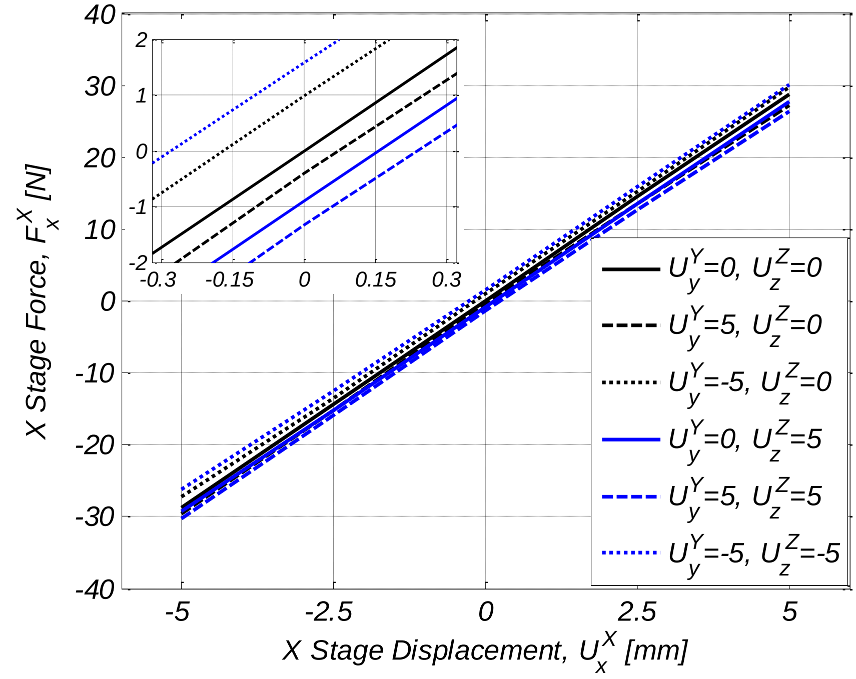

Fig.20 X Direction Force-Displacement Relation

The small shifts in the force-displacement line (inset) in the presence of U_y^Y and U_z^Z are caused by moments resulting from actuation forces that are applied away from the center of stiffness. A positive Y force at the Y stage moves the X stage very slightly in the positive X direction, and vice versa, which is manifested via the shift in the stiffness curve (black dashed line in Fig.20). The force is applied away from the center of stiffness, causing a positive moment about the Z axis. The relatively low torsional stiffness of the green PFMs about the Z axis allow some rotation, resulting in a small displacement in the positive X direction. A positive Z force at the Z stage moves the X stage very slightly in the positive X direction (more so than a positive Y force at the Y stage), and vice versa, which is manifested via the shift in the stiffness curve (solid blue line in Fig.20). The force is applied away from the center of stiffness, causing a positive moment about the Y axis. The relatively low torsional stiffness of the blue PFMs about the Y axis allows some rotation, resulting in a small displacement in the positive X direction.

Although not plotted here, the Y and Z direction stiffness also exhibit a similar behavior because of the symmetric design. This validates the unique attribute of the proposed flexure mechanism that its mobility in one direction is not influenced by motion in the other directions. This decoupling allows large motions in each direction, unconstrained by the geometry and limited only by material failure.

Fig.21 captures the X direction motion that is 'lost' between the point of actuation and the point of interest. It is also inversely related to the transmission stiffness, which represents the stiffness between the point of actuation and point of interest and is critical in high-speed, motion control applications. The difference between U_x^{XYZ} and U_x^X is plotted over the entire range of X actuation for different values of the Y actuation (U_y^Y). Because this lost motion is found to be largely insensitive to the Z actuation (U_z^Z) the curves in Fig.21 are plotted for U_z^Z = 0 *mm* only.

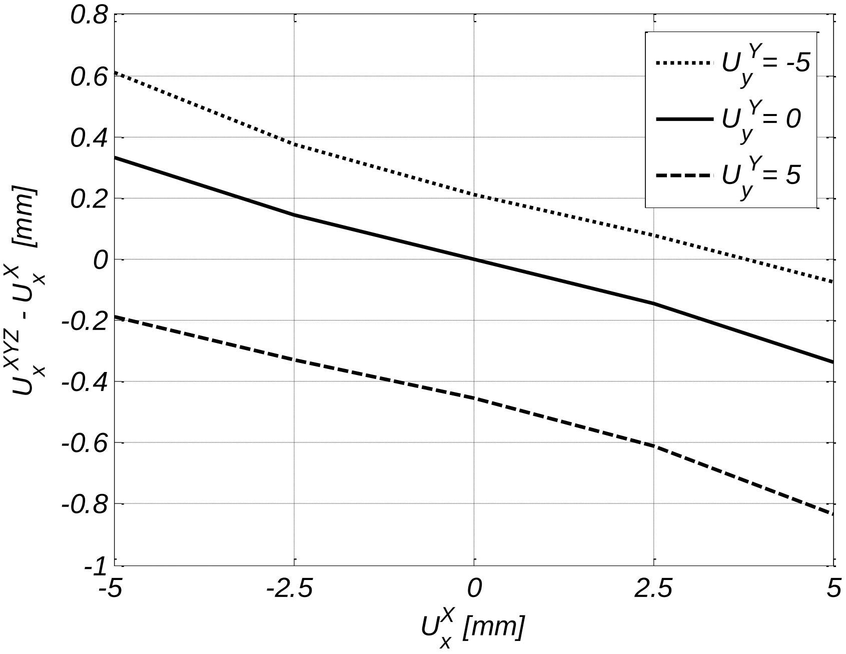

Fig.21 X Direction Lost Motion vs. U_x^X

When U_y^Y and U_z^Z actuation are zero, the lost motion varies nearly linearly with U_x^X. As previously shown in Fig.20, the U_x^X varies linearly with F_x^X. Because the center of stiffness is not varying much with U_x^X, the subsequent moment also varies linearly with U_x^X. The relatively low torsional stiffness of the green PFMs about the Z axis allow a small amount of rotation about the positive Z axis. Therefore, this rotation also varies linearly with U_x^X. The blue PFMs remain nearly straight due to their relatively large shear stiffness, and the resulting lost motion varies linearly with the sine of this angle. The rotation is small (maximum 2.6 mrad), so the sine of the angle can be approximated as the angle alone. Therefore, the lost motion varies nearly linearly with U_x^X, as shown in Fig.21. The small nonlinearity (increasing rate of lost motion with U_x^X) arises from the varying torsional stiffness of the green PFMs with displacement. As they deform, their torsional stiffness decreases (see Fig.18), allowing more rotation and consequently displacement as can be seen in Fig.22. The X direction lost motion varies from 0.6 *mm* when U_x^X and U_y^Y are both -5 *mm* to -0.84 *mm* when U_x^X and U_y^Y are both 5 *mm*.

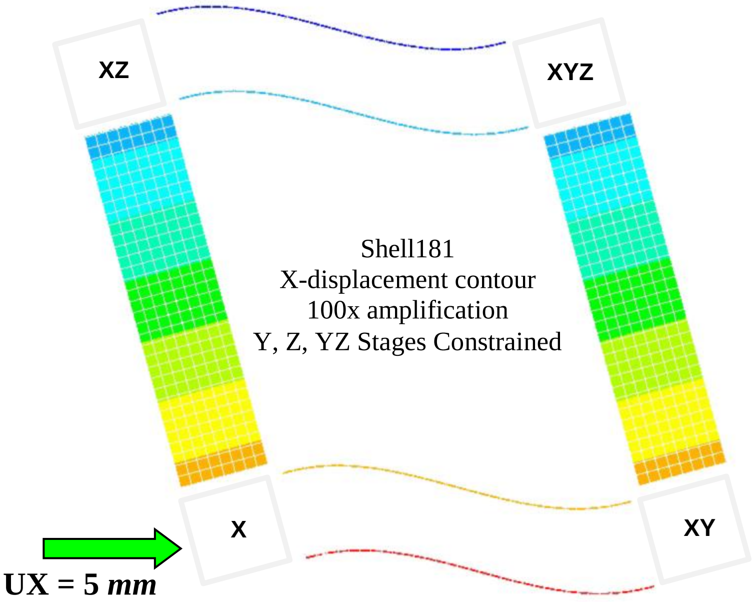

Fig.22 Lost Motion due to Lack of Torsional Stiffness

Fig.23 provides further insight into the lost motion by plotting the difference between U_x^{XYZ} and U_x^X over the entire range of U_y^Y for different values of U_x^X. The lost motion in the X direction has both a quadratic component and a linear component with respect to U_y^Y. The quadratic component arises from the arc-length conservation of the red PFMs, as can be seen alone in Fig.26. The linear component comes from the moment about the Z axis, arising from the application of the actuation force away from the center of stiffness. The relatively low torsional stiffness of the green PFMs allows a positive moment to produce a positive rotation about the Z axis. This rotation causes the X stage to have a translational component in the positive (absolute) X direction, and the XYZ stage to have a translational component in the negative (absolute) X direction, resulting in additional lost motion.

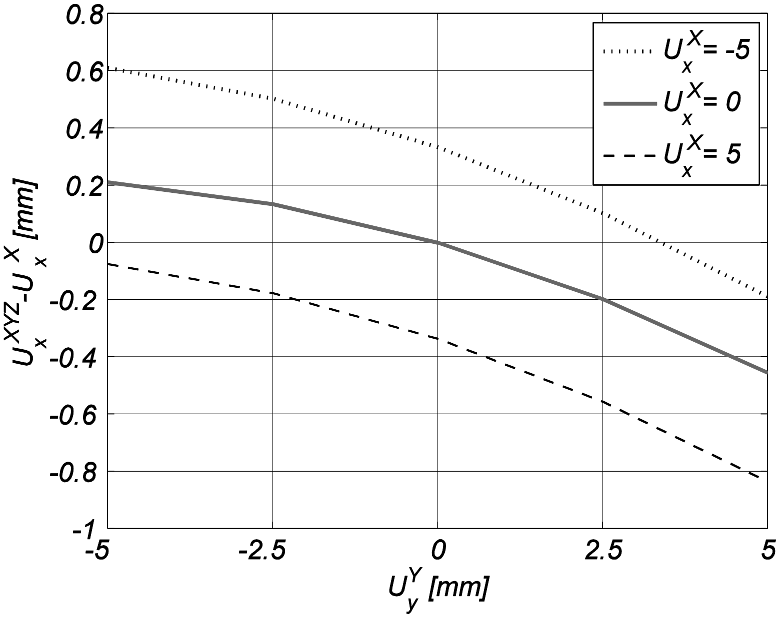

Fig.23 X Direction Lost Motion vs. U_y^Y

Next, the cross-axis error, which represents any motion of the XYZ stage in one direction caused by actuation in a different direction, is illustrated in Fig.24. The error in X direction is mathematically given by the difference between the actual X displacement of the XYZ stage (U_x^{XYZ}) in the presence of Y and Z actuation (U_y^Y and U_z^Z) and the nominal X displacement of the XYZ stage (U_x^{XYZ}) in the absence of Y and Z actuation is plotted. Thus, $U_x^{XYZ} - \left\{ U_x^{XYZ} \left(@U_y^Y = U_z^Z = 0 \right) \right\}$ is plotted over the entire range of U_y^Y for three values of U_z^Z. Since, this error motion is found to be largely insensitive to X actuation (U_x^X), the curves in are plotted for $U_x^X = 0$ *mm* only.

By definition, the cross-axis error motion is identical to the lost motion in response to Y actuation for U_x^X held at 0 *mm*. The cross-axis error in the X direction has both a quadratic component and a linear component with respect to U_y^Y. The quadratic component arises from the arc-length conservation of the red PFMs, as can be seen alone in Fig.26. The linear component comes from the moment about the Z axis, resulting from the application of the actuation force away from the center of stiffness. The relatively low torsional stiffness of the green PFMs allows a positive moment to produce a positive rotation about the Z axis. This rotation causes the XYZ stage to have a translational component in the negative X direction. The cross-axis error motion in X direction varies from a maximum value of 0.25 *mm* when U_y^Y is –5 *mm* and U_z^Z is 5*mm* to –0.53 *mm* when U_y^Y is 5 *mm* and $–U_z^Z$ is 5 *mm*. Due to symmetry, the same trend is observed for the Y and Z direction cross-axis errors.

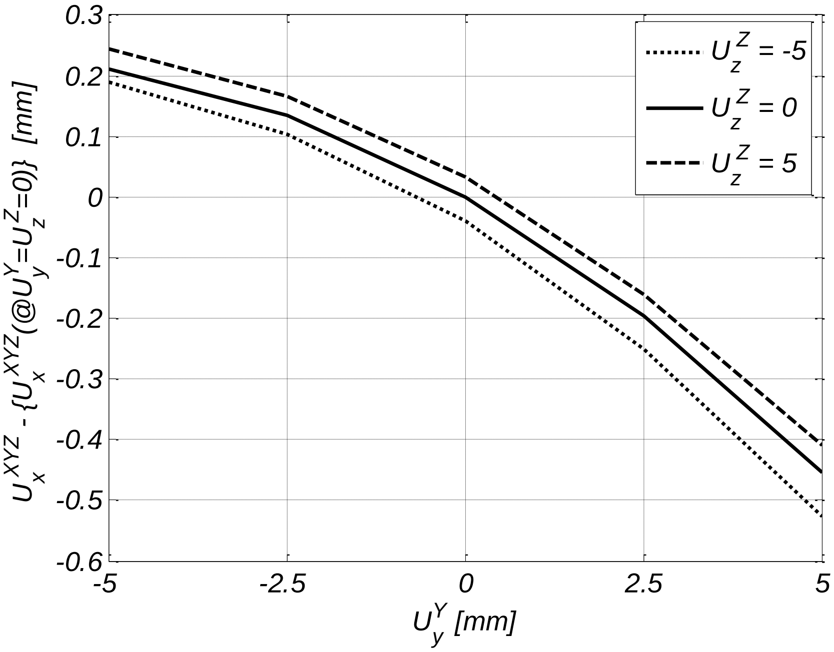

Fig.24 X Direction Cross-Axis Error Motion

Actuator isolation in a multi-axis flexure mechanism ensures that the point of actuation in any given direction moves only in that direction and is not influenced by actuation in the other directions. Fig.25 and Fig.26 show the Y and Z direction displacements of the X stage, U_y^X and U_z^X, respectively. For different values of Y actuation (U_y^Y), the Y direction displacement of the X stage (U_y^X) is plotted over the entire range of Z actuation (U_z^Z) in Fig.25.

Since this motion is found to be largely insensitive to X actuation, the curves are plotted for $U_x^X = 0$ *mm* only. The displacement of the X stage in the Y direction (U_y^X) has a predominant dependence on the Z actuation, which arises due to a lack of adequate shear stiffness of the green PFMs. The Z actuation is applied away from the center of stiffness, and creates a moment about the X axis. This moment causes the green PFMs to shear and displace in the Y direction. The maximum Y direction motion of the X stage is 0.073 *mm* when U_y^Y is 5 *mm* and U_z^Z is –5 *mm*, and –0.073 *mm* when U_y^Y is –5 *mm* and U_z^Z is 5 *mm*.

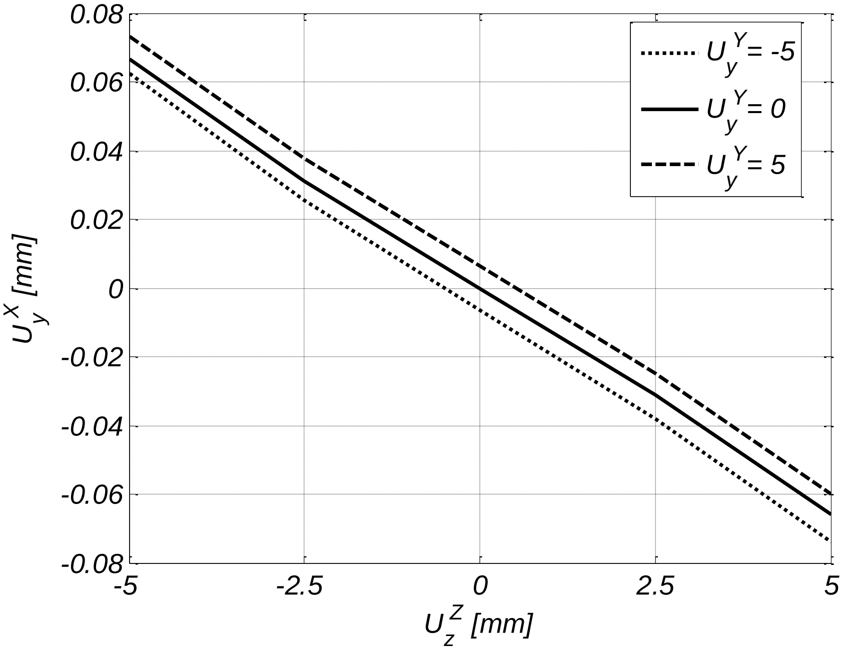

Fig.25 X Actuator Isolation (Y Direction)

Fig.26 shows the Z direction displacement of the X stage (U_z^X) over the entire range of X actuation (U_x^X). Since this motion is found to be largely insensitive to both Y and Z actuations, the curve is plotted for Y and Z actuations held at 0 *mm*. The Z direction displacement of the X stage (U_z^X) is primarily due to the kinematic arc-length conservation of the green PFMs, and therefore has a quadratic dependence on the X direction displacement of the X stage. The maximum Z direction motion of the X stage is –0.148 *mm* when U_x^X is ±5 *mm*.

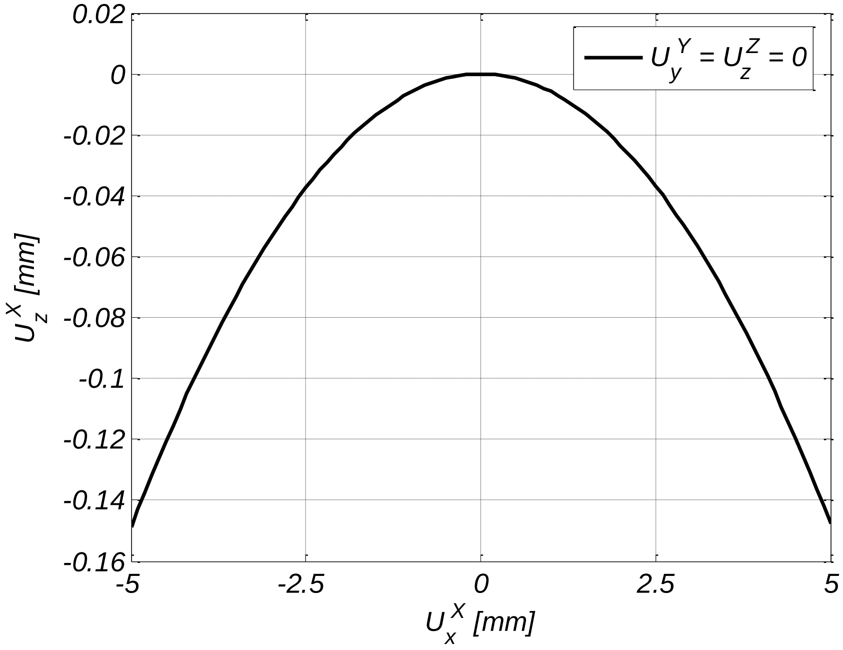

Fig.26 X Actuator Isolation (Z Direction)

In an XYZ flexure mechanism, all rotations are undesired and represent parasitic errors. Fig.27 shows the XYZ stage rotations about the X direction (θ_x^{XYZ}) over the entire range of Y actuation for three different Z actuations. The rotation varies primarily with Y and Z actuations, which produce twisting moments at the XYZ stage. It is largely insensitive to X actuation because the X direction force cannot create a moment about the X axis. Since this rotation is found to be largely insensitive to X actuation (U_x^X), the curves are plotted for U_x^X held at 0 *mm*. The rotation is linear with Z actuation because it is allowed by the relatively low torsional stiffness of the red PFMs. As described earlier, the Z actuation causes a moment about the X axis that is directly proportional to Z displacement. The red PFMs have a constant torsional stiffness with Z actuation, and therefore deflect linearly with the displacement. Similarly, the Y actuation produces a moment about the X axis. However, the X rotation has a nonlinear component with respect to Y actuation. This is because the torsional stiffness of the red PFMs decreases with Y displacement. This decrease in stiffness allows additional rotation as can be seen by the increasing slope of the lines in Fig.27.

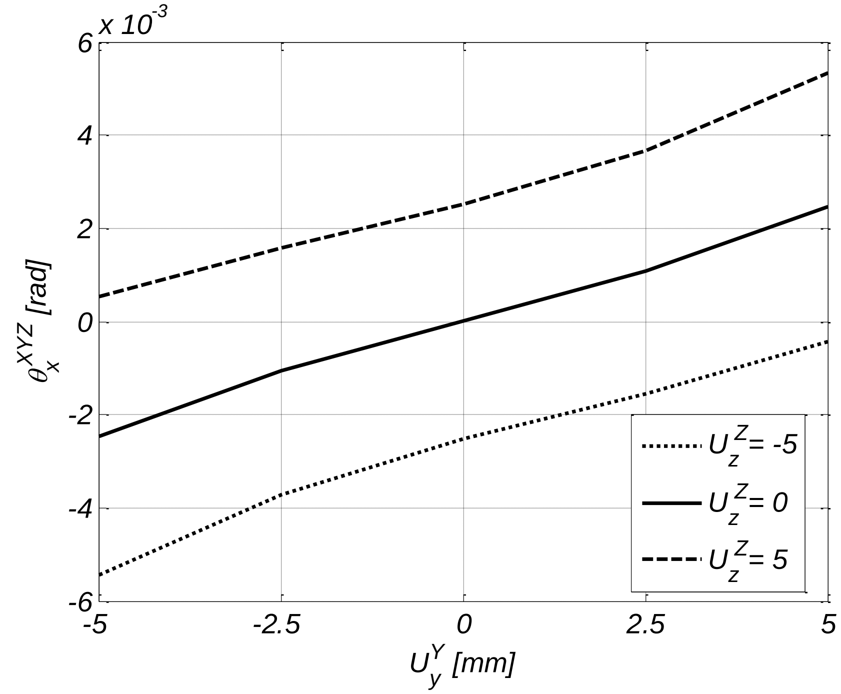

Fig.27 X Direction Rotation of the XYZ Stage

The maximum X direction rotation of the XYZ stage varies between a maximum positive value of 5.4 *mrad* when U_y^Y and U_z^Z are both 5 *mm* to a maximum negative value of –5.4 *mrad* when U_y^Y and U_z^Z are both –5 *mm*. Because of design symmetry, the XYZ stage rotation about the Y direction (θ_y^{XYZ}) depends similarly on the X and Z actuation but not as much on the Y actuation. And, the XYZ stage rotation about the Z direction (θ_z^{XYZ}) depends on the X and Y actuation, but not as much on the Z actuation.

These FEA results help highlight the extent of non-linear behavior in the mechanics of the proposed flexure mechanism design. Below, I summarize the FEA based motion performance of the proposed XYZ flexure mechanism, with the chosen dimensions:

i. 10 *mm* motion range in each direction, with the stiffness remaining invariant with actuation along the other two directions.
ii. Lost motion per axis less than 1.44 *mm* over the entire motion range (< 14.4% of range).
iii. Cross-axis error less than 0.78 *mm* over the entire motion range (< 7.8% of range).
iv. Actuator isolation less than 0.15 *mm* in any given direction over the entire motion range (< 1.5% of range).
v. Parasitic rotations of the XYZ stage less than 3.7 *mrad* over the entire motion range.

4.3 Mechanism CAD Design

As described in the previous chapter on conceptual design, the XYZ flexure mechanism cannot be manufactured monolithically from a single block of raw material. Therefore, it was designed in a modular fashion to allow for accurate and repeatable manufacturing and assembly. Extending from the lessons learned through the design, fabrication, and assembly of the first two prototypes, I focused on minimizing mass and total number of parts while simultaneously increasing the alignment accuracy of the entire assembly.

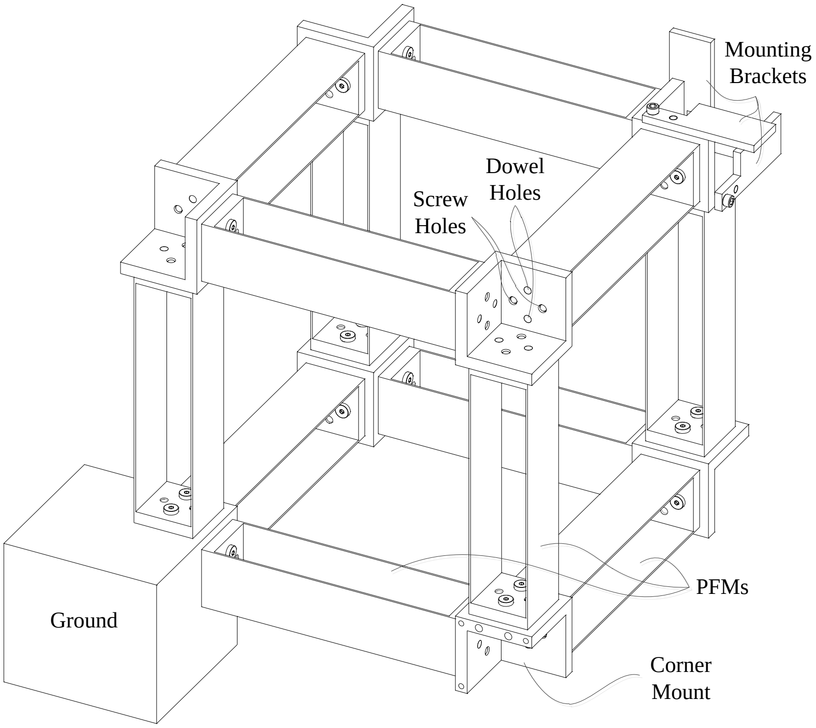

Fig.28 First CAD Concept for Detailed Design

CAD concepts were generated using monolithic PFMs as the primary building blocks, and iterated to reach the final design. The first concept uses separate intermediate stages to align and constrain the PFMS as shown in Fig.28. Each end of the PFMs are aligned with respect to the intermediate stages using two dowel features, and constrained using two screws. However, this method of alignment is over-constraining, and therefore, subject to manufacturing tolerances. Furthermore, assembly of the mechanism is cumbersome because the dowel pins must be pressed after all of the pieces are aligned.

The second concept, shown in Fig.29, incorporates alignment features into the rigid end plates of the PFMs, eliminating the need for additional intermediate stage parts. This attachment method is an extension of the first proof-of-concept design from Chapter III. However, shoulder bolts were incorrectly chosen to simultaneously align and constrain the rigid end plates. While the shoulder portion of the bolts provides a good alignment feature, the threads are only designed to provide a clamping force, negating this source of alignment.

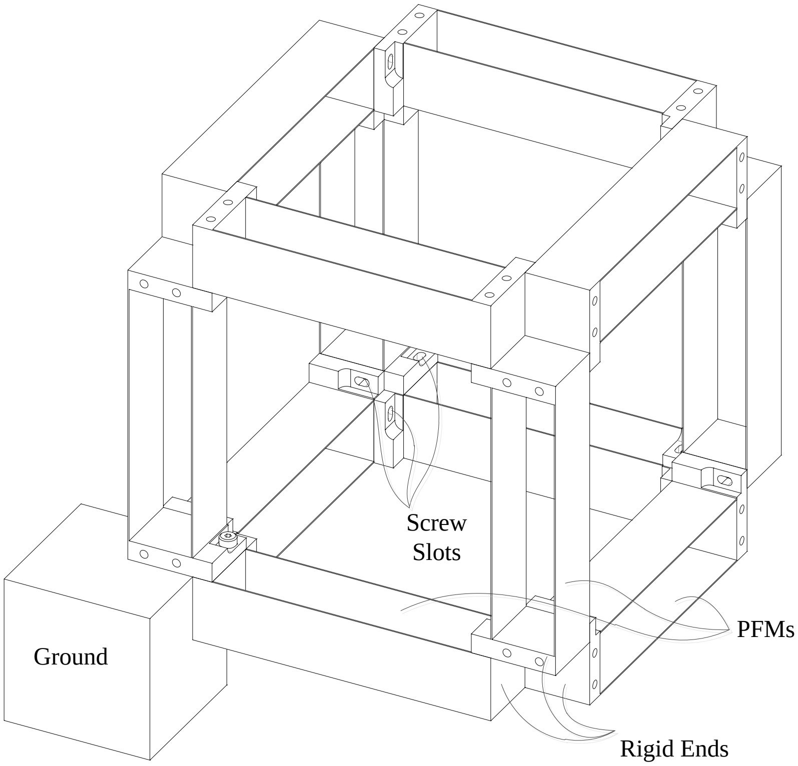

Fig.29 Second CAD Concept for Detailed Design

The second concept was iterated several times to eliminate over constraint and provide adequate alignment features. Ultimately, a concept was generated in which an interface between dowel pins and slots provide an exact constraint method of aligning three perpendicular PFMs without the need of an external jig. As shown in Fig.30, three rigid plates from three PFM modules come together at each corner of the flexure mechanism; the three plates are exactly constrained with respect to each other by means of dowels and mating slots. The slots prevent the assembly from being over-constrained, and accurately align the PFMs as they are tightened together with screws. The same dowel and screw features enable precise mounting of external sensors and actuators to the flexure mechanism.

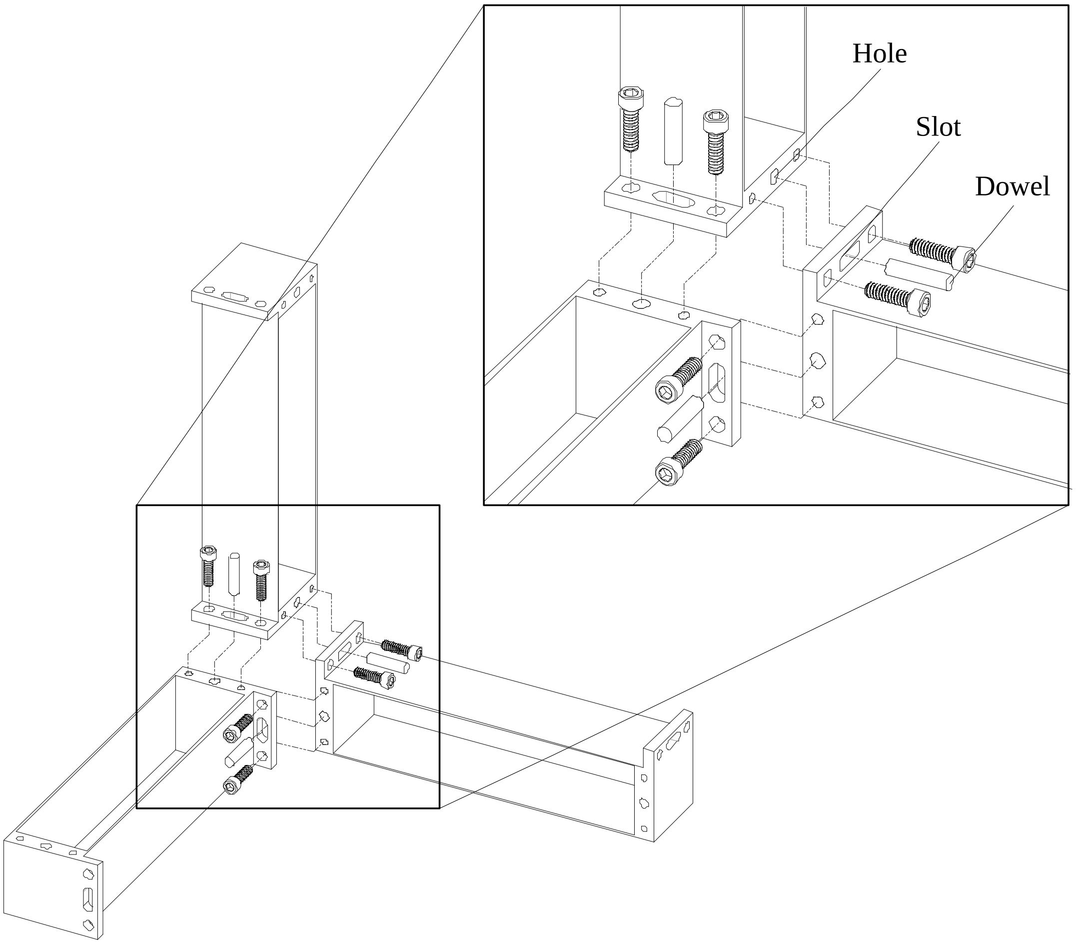

Fig.30 Method of Exact Constraint for PFM Alignment

This concept was validated with a quick prototype consisting of three perpendicular plates to represent the rigid ends of the PFMs. As the screws are tightened, drawing the three perpendicular surfaces together, the dowels slide along the slots ensuring exact constraint. Friction hinders the required sliding motion when the plate surfaces contact. Therefore, best alignment is achieved by repeatedly loosening and tightening the screws by a small amount until no further relative motion between the plates can be seen. Lubricating oil can also aid in this process.

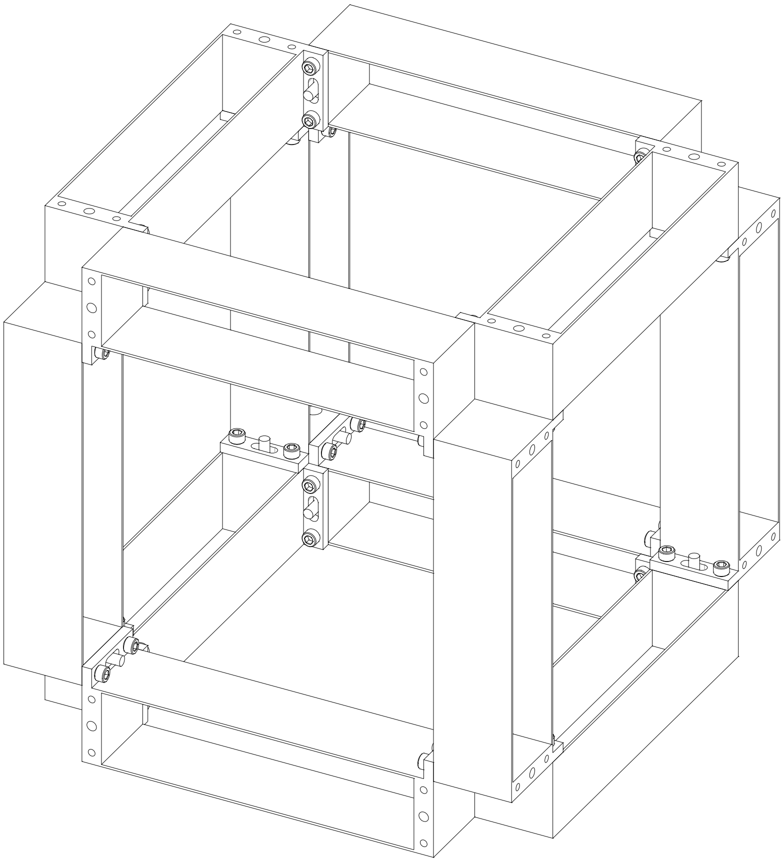

Fig.31 Entire Flexure Mechanism Assembly

The final flexure mechanism assembly is shown in Fig.31. It is consists of 12 identical PFMs held together by 1/8 *in* dowel pins and 4-40 machine screws. For mounting the mechanism to a rigid ground, the external dowel and screw holes could be used. However, because the mechanism will be subjected to large external loads, I added larger dowel and screw holes on the end of one of the PFMs to provide a stronger constraining force.

The PFMs were fabricated using a combination of wire electric discharge machining (EDM) and CNC milling. Details on the tolerances and fabrication procedure of the PFMs can be found in APPENDIX A. Design of an experimental setup, as well as a nanopositioning setup, is discussed in the subsequent chapters.

CHAPTER V

Experimental Validation

5.1 Design of Experiment

An experimental setup, shown in Fig.32, was designed and fabricated to validate the qualitatively predicted motion performance of the proposed flexure mechanism. The important measurements include actuation stiffness, cross-axis error motion, actuator isolation, and XYZ stage rotation. These measurements require measurements of the absolute translational and rotational displacements at the X, Y, Z, and XYZ stages.

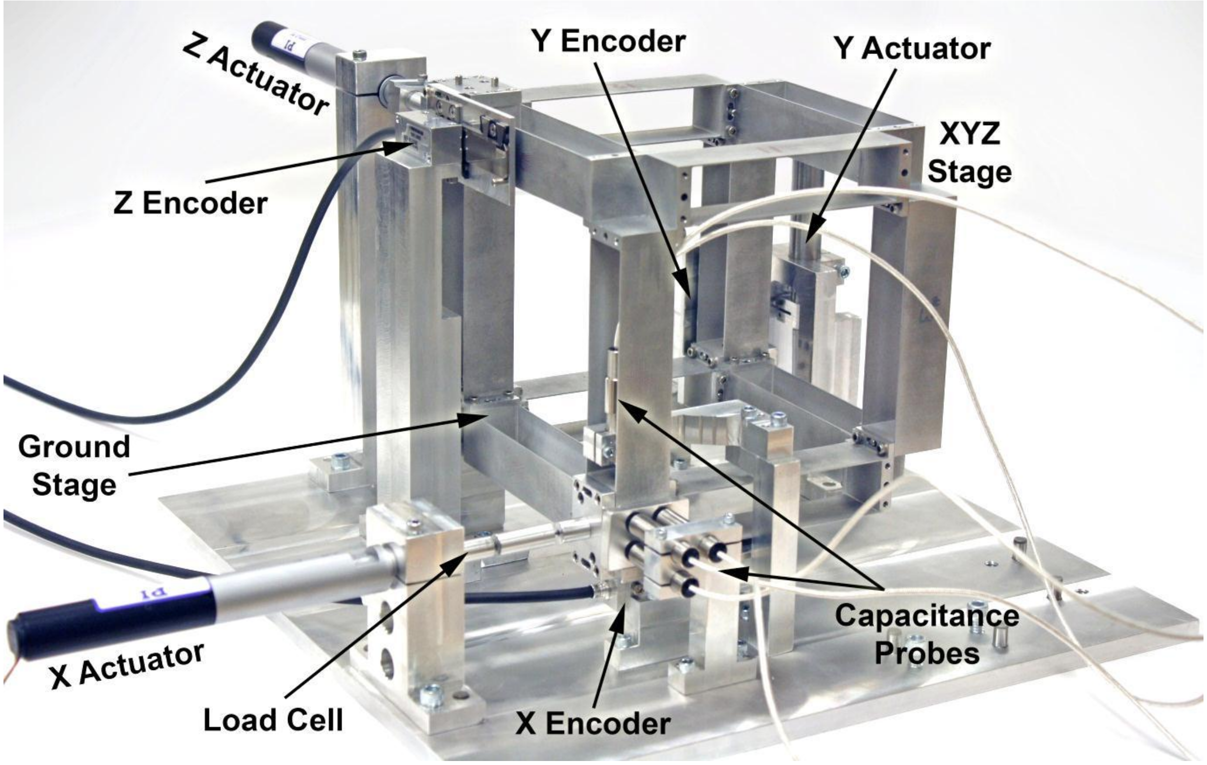

Fig.32 Experimental Setup

High-resolution linear optical encoders are well-suited for measuring long range single-axis translations of the X, Y, and Z stages. Renishaw encoders (RELM scale, Si-HN-4000 readhead, and SIGNUM interface) are capable of *5 nm* resolution, *80 mm* measurement range, and off-axis tolerance of 250 μm. Given the symmetry of the design, the error motions associated with an actuation stage are measured at the X stage only. Since these error motions are relatively small (≤ 150 *μm*), an arrangement of five capacitance probes is used to measure the Y and Z translations and the three rotations at the X stage. Similarly, the cross-axis errors and parasitic rotations at the XYZ stage are also measured using multiple capacitance probes. Lion Precision capacitive probes (model # C1A) are capable of a 10 *nm* resolution over a *500 μm* range at *15 KHz* bandwidth. The force applied at the X stage is measured using a load cell. A Measurement Specialties load cell (ELFF-T4E-20L-/V10) is capable of both tension and compression measurements up to 50 *N* with ±0.5% nonlinearity and hysteresis. The X stage is actuated with a PI DC micrometer (M-227.25) in closed-loop for repeatability. The Y and Z stages are manually positioned using micrometers.

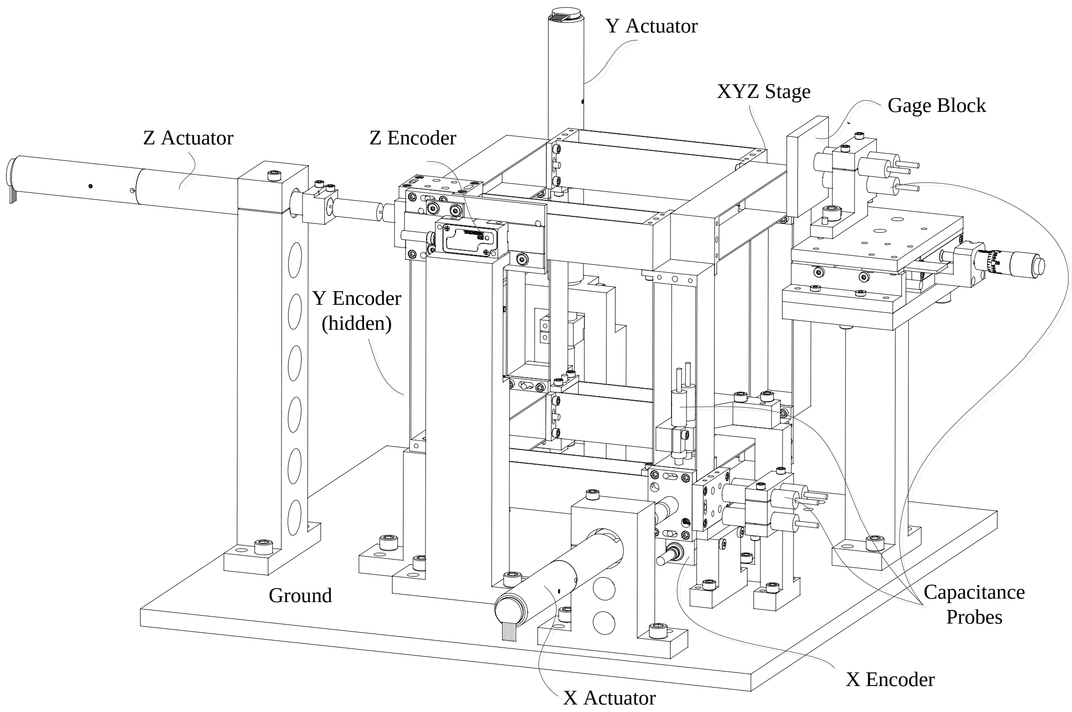

Fig.33 CAD Model of Experimental Setup

Fig.34 shows the components of the X actuator sub-assembly, including the load cell. The DC Mike actuator is attached to the load cell through an adapter that clamps the tip of the DC Mike on one side and threads the load cell on the other end. Next a decoupler attaches the load cell to the actuation stage mount. The decoupler is designed to transmit the actuation force along the actuation direction while isolating the DC Mike and load cell from the off-axis motions of the actuation stage.

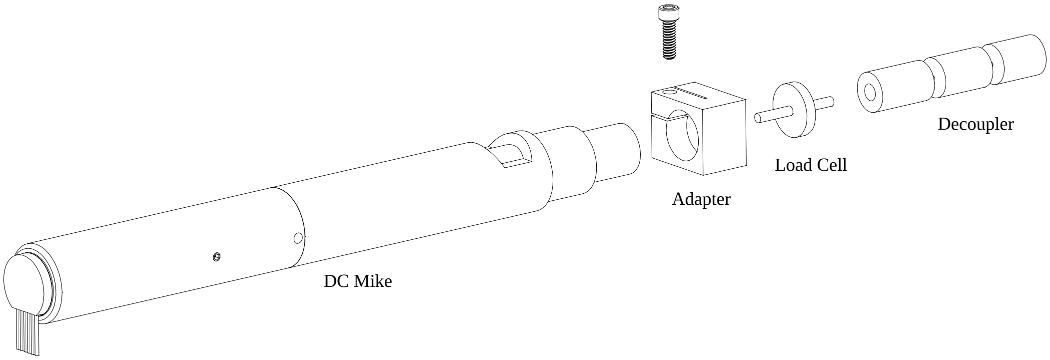

Fig.34 X Actuator Sub-Assembly with Load Cell

The “hourglass” decoupler is constructed of three rigid sections and two piano wire flexures as shown in Fig.35. The two end sections are threaded to allow for attachment with 10-32 screws. The length and thickness of the flexible sections were chosen based on buckling and yield criteria for the expected loads with a safety factor of 2. Additionally, the off-axis forces were minimized within the given constraints. Similar decouplers are also designed for the Y and Z stages without threads for a load cell.

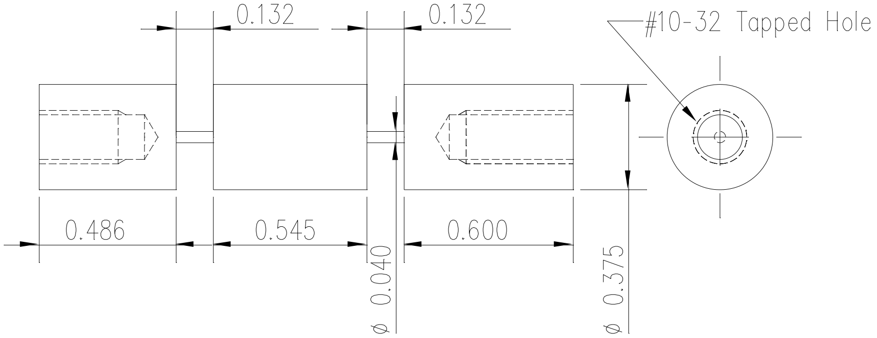

Fig.35 Hourglass Decoupler

In order to accurately and repeatedly assembly and align all of the components, the sensor and actuator mounts are all screwed into a common ground plate and each is aligned with two clearance fit dowels.

The actuator mounts are designed such that the maximum expected actuation force will not bend the mount by more than 0.1% of the actuation range, or 5 *μm*. With the Z actuator mount being the longest cantilever, the corresponding beam thickness is 1 *in*. To minimize raw material consumption and machining work, the X actuator mount was also made to 1 *in* thickness. The Y actuator mount is designed to save space by mounting the Y actuator in an inverted position, slightly offset from the Y stage. A rigid mounting arm attaches the Y actuator to the Y stage. This slight offset will add a small additional moment that was not included in the FEA.

The sensor mounts do not need to bear loads like the actuator mounts, and can therefore be made much smaller. The encoder readheads attach to the mounts by clamping the side surface with two screws. With clearance holes in the mounts, the two mating surfaces allow 3 DoF of adjustment. However, the position and parallelism of the readheads and encoder strips are not adjustable, and must be ensured through tight machining tolerances. The capacitance probes are mounted in precision-reamed, “C-clamp” style holes. They measure the absolute distance to gage blocks that are glued to the sides of the flexure mechanism stages.

5.2 Design Lessons Learned

The entire assembly works reasonably well, but has a few shortcomings. First, the alignment of each mount relative to the ground plate is achieved with two dowel pins locating two dowel holes. This type of assembly is over-constrained, and very susceptible to manufacturing tolerances. A better method of alignment consists of three dowel pins locating two surfaces. This is exactly constrained, and allows for small irregularities in manufacturing.

Second, the joining of each mount relative to the ground plate is accomplished by screwing through clearance holes in the mounts into the ground plate. This method was chosen to allow assembly by one individual on a table, as well as to allow easy removal of mounts for different sensor setups or repair. However, some of the sensor mounts are in close proximity to each other and to the bearing, making access to some screws difficult, if not impossible without the proper tools. Additionally, screwing from above required the design and fabrication of mounting tabs on every mount which greatly increased the design complexity, fabrication time and cost, and material waste. To overcome all of these drawbacks, the mounting designs could all be altered to simple, rectangular extrusions with screws coming up through the base into each mount.

Next, as previously described, the encoder readhead mounts do not allow for the full 5 DoF adjustments necessary to precisely align the readhead to the encoder stip. With the stacked tolerances from the readhead, readhead mount, ground, bearing mount, bearing PFM, encoder strip mount, and encoder strip, the misalignment due to manufacturing tolerances was too great to even use the optical encoders as-is. The mounting dowels were removed and shims were used to attain proper alignment, but this resulted in several hours of work for each sensor every time the setup was moved. To alleviate this problem, the mount should be designed with no alignment dowels, but instead with additional screws to allow the additional DoF. One example is to have one screw clamping the mount and three screws pressing against the mount to adjust height, pitch, and roll. Combined with the three DoF allowed between the mount and the ground, all 6 DoF would be available for fine adjustment with screws.

Another source of difficulty and uncertainty came from the hourglass flexures used to separate the actuators from the nonlinear motion of the bearing. While designed well in theory, the construction of the hourglass flexures was difficult to create from solid material. The resulting flexures were made from four separate pieces that did not remain solid throughout the series of experiments. This resulted in inconsistencies between tests. A good solution is to determine a fabrication method that would allow the manufacturing of the flexures from a single piece of material, or to otherwise permanently join the flexible and rigid sections.

Finally, the C-clamps used to mount the actuators and cap probes showed signs of fatigue over time, and did not provide strong, even clamping force around the delicate bodies of the actuators and cap probes. A simple solution is to replace the C-clamps with split-rings and set screws. This would provide a more durable mounting platform that can provide greater clamping force without damaging the equipment.

5.3 Procedure

Four different sensor setups and testing procedures are required to gather all of the pertinent data. For each test, the three linear optical encoders and the load cell take measurements from the same positions. However, the lab has only three of the required capacitance probes, necessitating movement of the sensors between the four mounting locations. First, three probes are mounted at the X stage in the Z direction to measure the Z translation and X and Y rotations. Second, two probes are mounted at the X stage in the Y direction to measure the Y translation and Z rotation. Third, three probes are mounted at the XYZ stage in the Z direction to measure the Z translation and X and Y rotations. Finally, three probes are mounted at the XYZ stage in the X direction to measure the X translation and Y and Z rotations.

Ideally, each setup is tested over the entire X, Y, and Z motion range of 10 *mm* x 10 *mm* x 10 *mm*. However, I discovered that the errors motions of the X, Y, and Z, stages forced the linear optical encoders out of alignment before the range limits were reached. Therefore, the tests were limited to a maximum range of ±3 *mm* in each direction.

With the Y and Z stages fixed, data are captured as the X stage stepped from 0 *mm* to +3 *mm* to -3 *mm* to 0 *mm* in 1 *mm* increments, as shown in Fig.36. This is repeated for all combinations of Y and Z stage locations of 0 *mm*, +2.5 *mm*, and -2.5 *mm*. Before testing at each new location, the three linear optical encoders must be realigned to guarantee good signal strength through the entire motion range. After all tests are completed for a given sensor setup, one additional test cycle is run with the Y and Z stages back at zero to check for any drift in the capacitance probe and load cell outputs. See APPENDIX B for a detailed testing procedure.

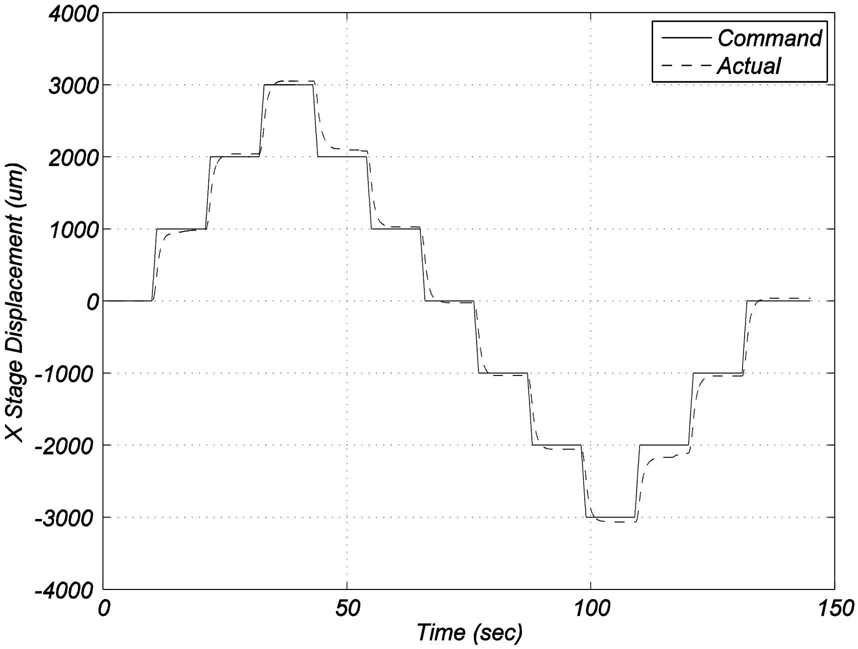

Fig.36 X Actuation Test Cycle

Before running the tests for each sensor setup, it is important to zero the X, Y, and Z stage positions. For the X stage, this can be done by reading the output from the capacitance probes pointing along the Z axis at the X stage. The stage is actuated until the distance from the capacitance probes is at its minimum. Zeroing the Y and Z stages is more difficult because there are no additional sensor mounts available. The best method of zeroing these stages is to place a gage block along one of the PFMs that has the same DoF as the actuation stage. As shown in Fig.37 a., there is a gap between the gage block and the flexure. The stage is zeroed by actuating until the gage block is perfectly flush along the length of the flexure as shown in Fig.37 b. For improved accuracy, begin with a gap at one end, actuate until light is no longer visible through the gap, and record the location output from the encoder. Next, actuate until a gap is visible on the other end, and repeat the same procedure, again recording the encoder position at which the gap is no longer visible. Finally, the zero position of the stage is the average of the two recorded encoder positions. With this method, I have achieved a range of 200 μm in which no gap is visible. Each new test records the stage position relative to the beginning of the test. By recording the relative stage position across all tests, the absolute position of the stage relative to the initial zero location is known.

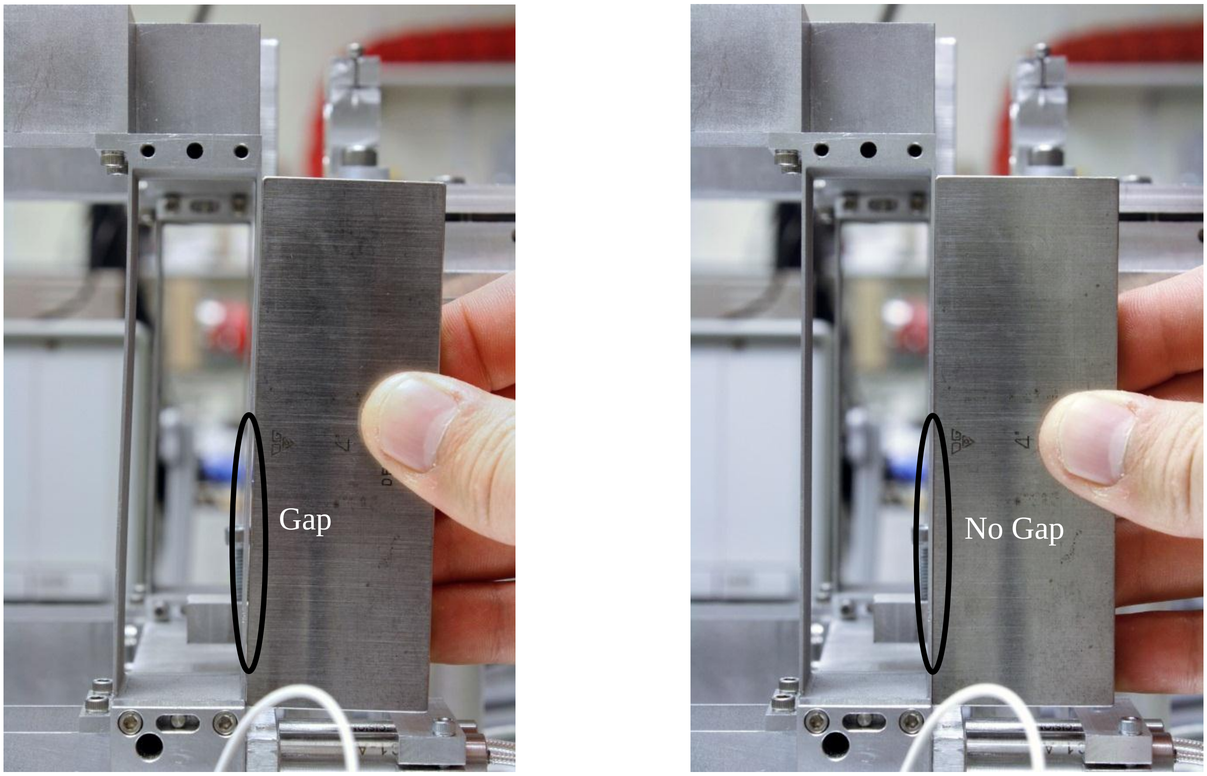

Fig.37 Flexure Alignment

The particular encoders used in the experimental setup cannot tolerate the off-axis motions produced throughout the entire range of the flexure mechanism. Therefore, the linear optical encoders must be aligned at the beginning of each test. Indicator lights on the readhead blink red when the encoder is out of range, remain solid red when the signal is weak, remain solid orange when the signal is moderate, and remain solid green when the signal is good. Additionally, Signum software on the computer can read more detailed information about the encoder's signal strength and readhead pitch. It is important to verify that readhead is perpendicular to the encoder strip within an appropriate gap, as shown in Fig.38. This ensures good data acquisition across the range of each test.

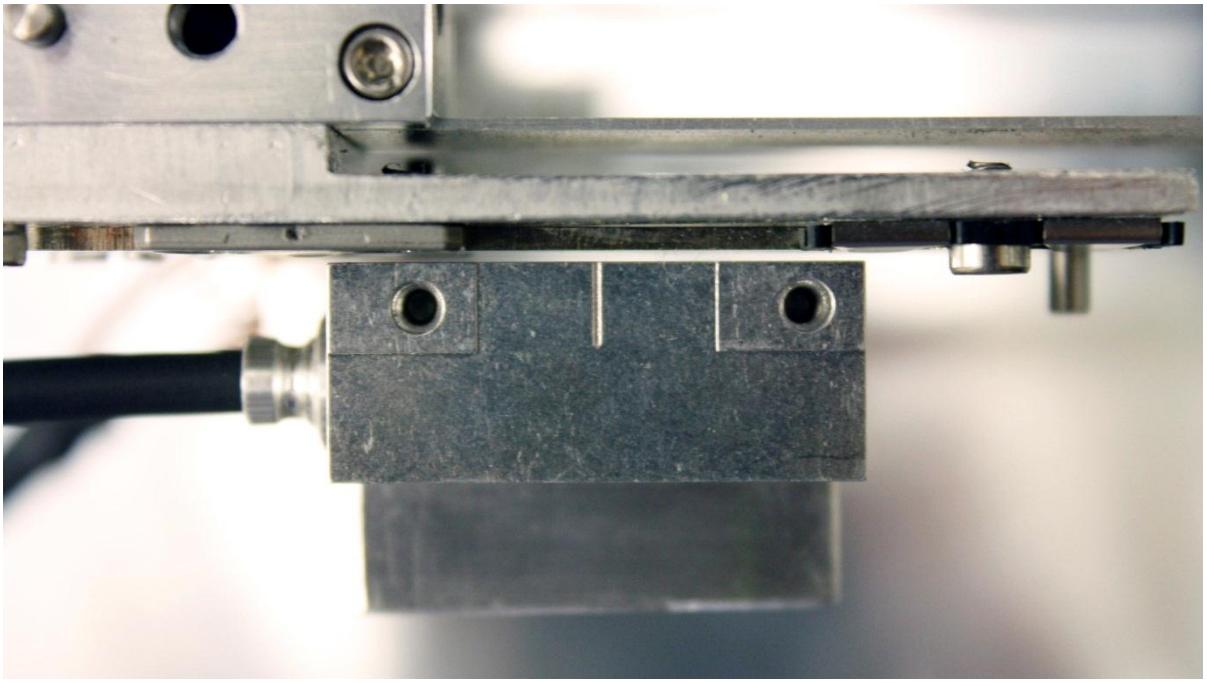

Fig.38 Optical Encoder Alignment

5.4 Results and Discussion

The following figures illustrate representative FEA results and experimental measurements. They demonstrate the geometric decoupling between the three axes, the resulting large, unconstrained motion range, and the small error motions. The FEA is displayed with black lines, and the experimental data is displayed with blue markers and polynomial fitted lines.

Fig.39 shows the stiffness associated with the X direction displacement of the X stage in response to an X direction force at this stage. This X direction stiffness is measured for various combinations of Y and Z stage actuations. The force-displacement curves are linear, as expected; however, the measured stiffness is about 1.5 times greater than the predicted stiffness. Additional FEA and experiments reveal minimal variance in the above X direction stiffness for all possible combinations of Y and Z stage displacements, confirming the highly decoupled motion.

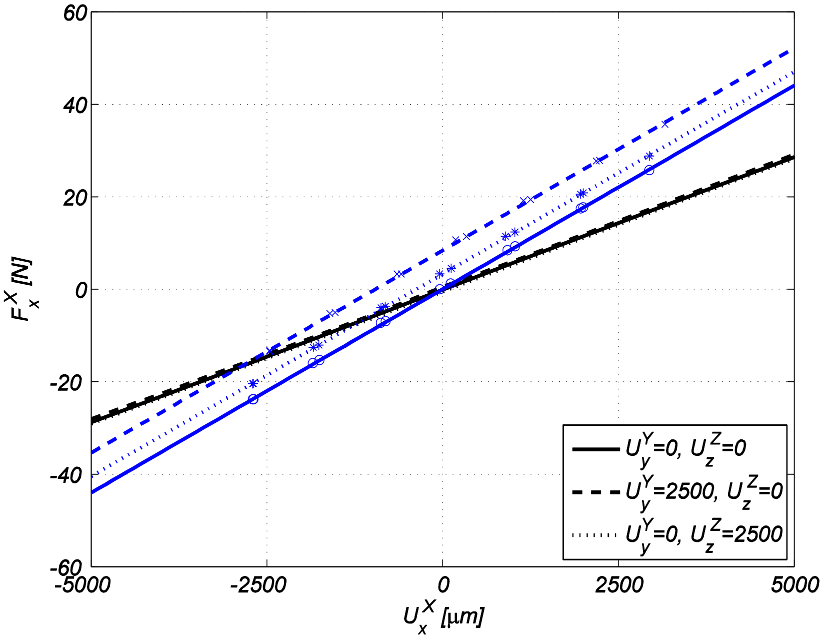

Fig.39 X Direction Force-Displacement Relation

The small shifts in the force-displacement lines in the presence of U_y^Y and U_z^Z are caused by moments resulting from actuation forces that are applied away from the center of stiffness. A positive Y force at the Y stage moves the X stage very slightly in the positive X direction, and vice versa, which is manifested via the shift in the stiffness curve. The force is applied away from the center of stiffness, causing a positive moment about the Z axis. The relatively low torsional stiffness of the green PFMs about the Z axis allow some rotation, resulting in a small displacement in the positive X direction. A positive Z force at the Z stage moves the X stage very slightly in the positive X direction (more so than a positive Y force at the Y stage), and vice versa, which is manifested via the shift in the stiffness curve. The force is applied away from the center of stiffness, causing a positive moment about the Y axis. The relatively low torsional stiffness of the blue PFMs about the Y axis allow some rotation, resulting in a small displacement in the positive X direction.

Fig.40 captures the X direction motion that is ‘lost’ between the point of actuation and the point of interest. It is also inversely related to the transmission stiffness, which represents the stiffness between the point of actuation and point of interest and is critical in high-speed, motion control applications. The difference between U_x^{XYZ} and U_x^X is plotted against X actuation for different values of the Y actuation (U_y^Y). Because this lost motion is found to be largely insensitive to the Z actuation (U_z^Z) the curves are plotted for $U_z^Z = 0$ *mm* only.

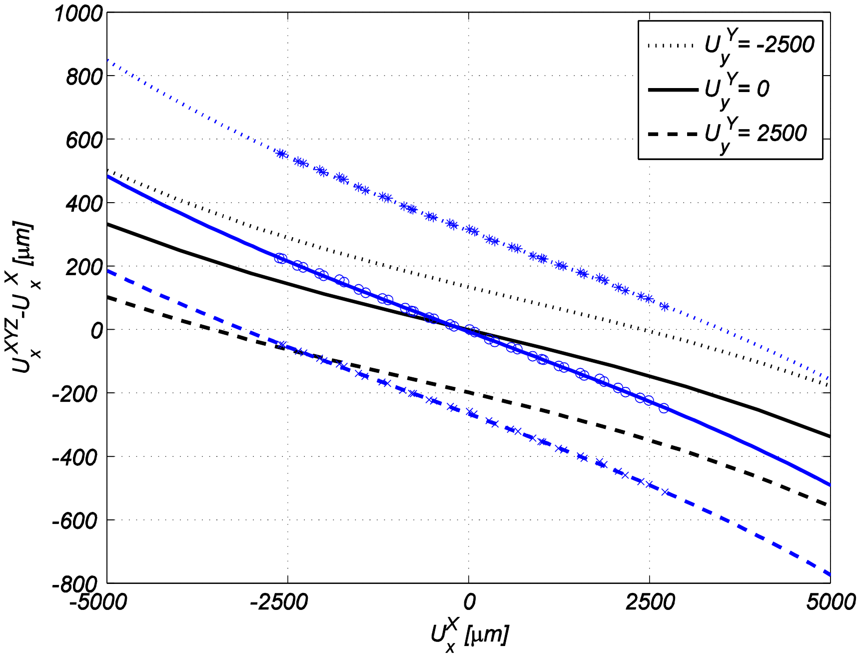

Fig.40 X Direction Lost Motion vs. U_x^X

When U_y^Y and U_z^Z actuation are zero, the lost motion varies nearly linearly with U_x^X. As previously shown in Fig.39, U_x^X varies linearly with F_x^X. Because the center of stiffness is not varying much with U_x^X, the subsequent moment also varies linearly with U_x^X. The relatively low torsional stiffness of the green PFMs about the Z axis allow a small amount of rotation about the positive Z axis. Therefore, this rotation also varies linearly with U_x^X. The blue PFMs remain nearly straight due to their relatively large shear stiffness, and the resulting lost motion varies linearly with the sine of this angle. The rotation is so small that the sine of the angle can be approximated as the angle alone. Therefore, the lost motion varies nearly linearly with U_x^X, as shown in Fig.40. The small nonlinearity (increasing rate of lost motion with U_x^X) arises from the varying torsional stiffness of the green PFMs with displacement. As they deform, their torsional stiffness decreases, allowing more rotation and consequently displacement. The X direction lost motion measurement varies from 528 *µm* when U_x^X is 2500 *µm* and U_y^Y is -2500 *µm* to -674 *µm* when U_x^X is -2500 *µm* and U_y^Y is 3000 *µm*.

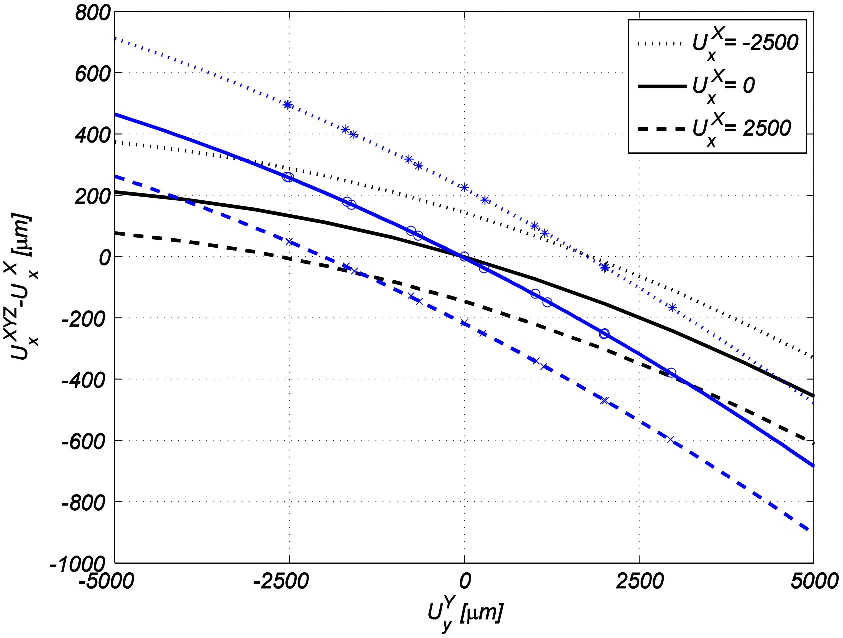

Fig.41 X Direction Lost Motion vs. U_y^Y

As predicted, the lost motion in the X direction has both a quadratic component and a linear component with respect to U_y^Y, as shown in Fig.41. The quadratic component, which is similar for both the experimental data and the FEA, arises from the arc-length conservation of the red PFMs. The linear component, however, differs between the experimental data and the FEA by a factor of 1.7, which is similar to the variance seen in the force-displacement relationship. This linear component comes from a moment about the Z axis, arising from the application of the actuation force away from the center of stiffness. The relatively low torsional stiffness of the green PFMs allows a positive moment to produce a positive rotation about the Z axis. This rotation causes the X stage to have a translational component in the positive (absolute) X direction, and the XYZ stage to have a translational component in the negative (absolute) X direction, resulting in additional lost motion.

The cross-axis error, which represents any motion of the XYZ stage in one direction caused by actuation in a different direction, is illustrated in Fig.42. Since, this error motion is found to be largely insensitive to X actuation (U_x^X), the curves in are plotted for $U_x^X = 0$ *mm* only. By definition, the cross-axis error motion is identical to the lost motion in response to Y actuation for U_x^X held at 0 *mm*. Therefore, the differences between the experimental data and the FEA are the same as in the lost motion plot with respect to U_y^Y. The cross-axis error motion in X direction varies from a maximum measured value of 264 *µm* when U_y^Y is –2470 *µm* and U_z^Z is -2500 µ*m* to –338 *µm* when U_y^Y is 2976 *µm* and U_z^Z is 2500 *µm*. This equates to cross-axis error motion in X direction that varies from a maximum value of 490 *µm* when U_y^Y is –5000 *µm* and U_z^Z is -5000 µ*m* to –680 *µm* when U_y^Y is 5000 *µm* and U_z^Z is 5000 *µm*.

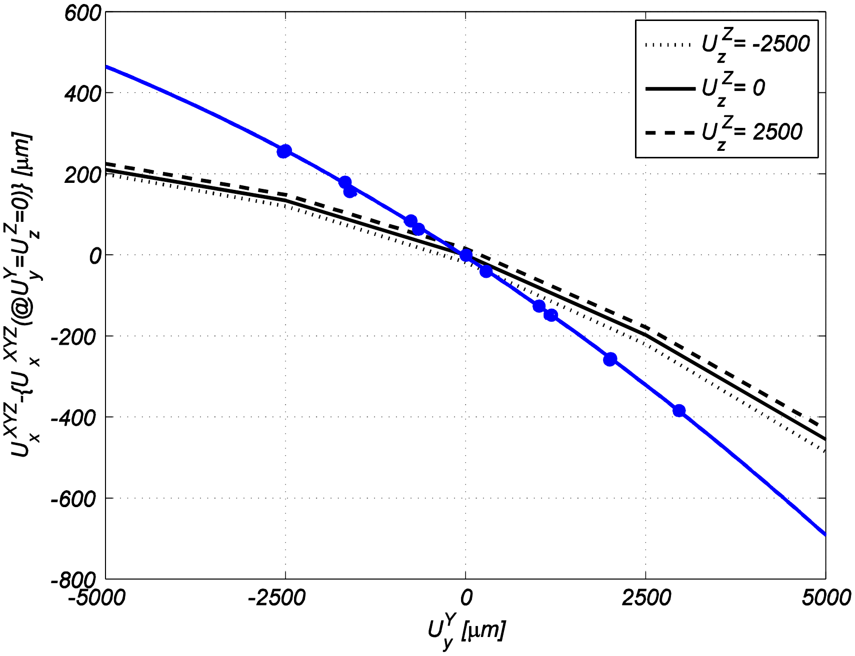

Fig.42 X Direction Cross-Axis Error Motion

Actuator isolation in a multi-axis flexure mechanism ensures that the point of actuation in any given direction moves only in that direction and is not influenced by actuation in the other directions. Fig.43 and Fig.44 show the Y and Z direction displacements of the X stage, U_y^X and U_z^X, respectively. For different values of Y actuation (U_y^Y), the Y direction displacement of the X stage (U_y^X) is measured against Z actuation (U_z^Z) in Fig.43. Since this motion is found to be largely insensitive to X actuation, the curves are plotted for $U_x^X = 0$ *mm* only. The results are highly linear, and differ between the experimental data and the FEA by a factor of 2.5. This discrepancy is likely due to the FEA model assumption of a monolithic construction and fails to account for the large, yet finite, joint stiffness associated with the interface of three PFMs at each corner of the assembled flexure mechanism.

The displacement of the X stage in the Y direction (U_y^X) has a predominant dependence on the Z actuation, which arises due to a lack of shear stiffness of the green PFMs. The Z actuation is applied away from the center of stiffness, and creates a moment about the X axis. This moment causes the green PFMs to shear and displace in the Y direction. The maximum measured Y direction motion of the X stage is 85 μm when U_y^Y is 2500 μm and U_z^Z is –2530 μm. This equates to a maximum Y direction motion of the X stage of 172 μm when U_y^Y is 5000 μm and U_z^Z is –5000 μm.

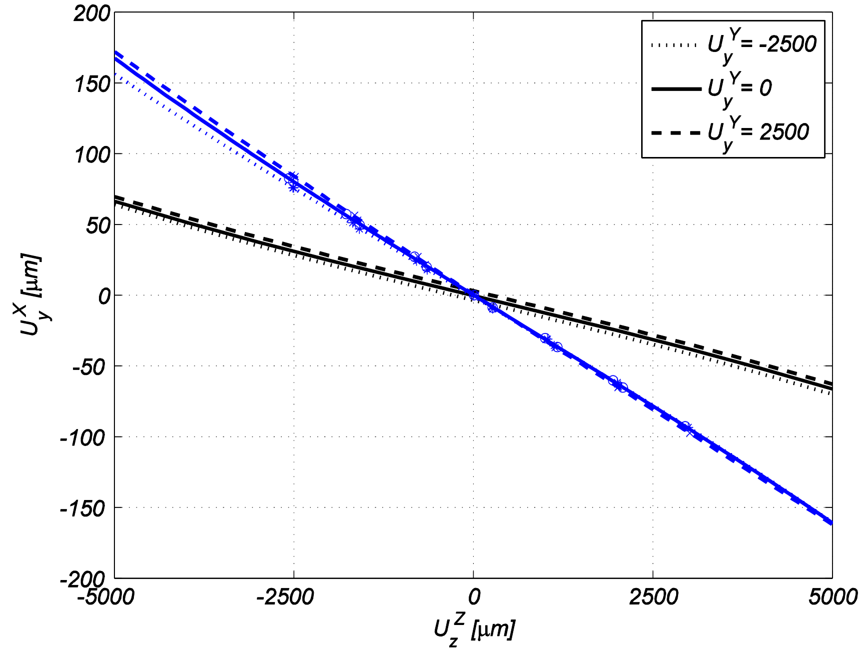

Fig.43 X Actuator Isolation (Y Direction)

Fig.44 shows the Z direction displacement of the X stage (U_z^X) over the entire range of X actuation (U_x^X). Since this motion is found to be largely insensitive to both Y and Z actuations, the curve is plotted for Y and Z actuations held at 0 *mm*. The Z direction displacement of the X stage (U_z^X) is primarily due to the kinematic arc-length conservation of the green PFMs, and therefore has a quadratic dependence on the X direction displacement of the X stage. The behavior is very well understood, and the experimental data varies from the FEA by only 9.2%. The maximum measured Z direction motion of the X stage is –47.8 μm when U_x^X is 2938 μm. This equates to a maximum Z direction motion of the X stage of -134.9 μm when U_x^X is ± 5000 μm.

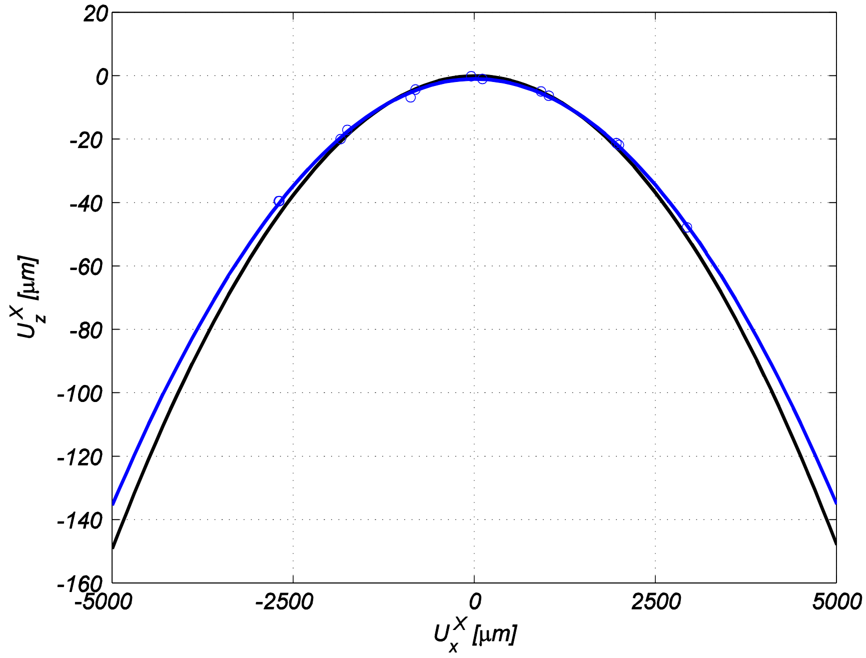

Fig.44 X Actuator Isolation (Z Direction)

Fig.45 shows the XYZ stage rotations about the X direction (θ_x^{XYZ}) against Y actuation for three different Z actuations. The rotation varies primarily with Y and Z actuations, which produce twisting moments at the XYZ stage. It is largely insensitive to X actuation because the X direction force cannot create a moment about the X axis. Since this rotation is found to be largely insensitive to X actuation (U_x^X), the curves are plotted for U_x^X held at 0 *mm*.

The rotation is linear with Z actuation because it is allowed by the relatively low torsional stiffness of the red PFMs. As described earlier, the Z actuation causes a moment about the X axis that is directly proportional to Z displacement. The red PFMs have a constant torsional stiffness with Z actuation, and therefore deflect linearly with the displacement. Similarly, the Y actuation produces a moment about the X axis. However, the X rotation has a nonlinear component with respect to Y actuation. This is because the torsional stiffness of the red PFMs decreases with Y displacement. This decrease in stiffness allows additional rotation as can be seen by the increasing slope of the lines in Fig.27.

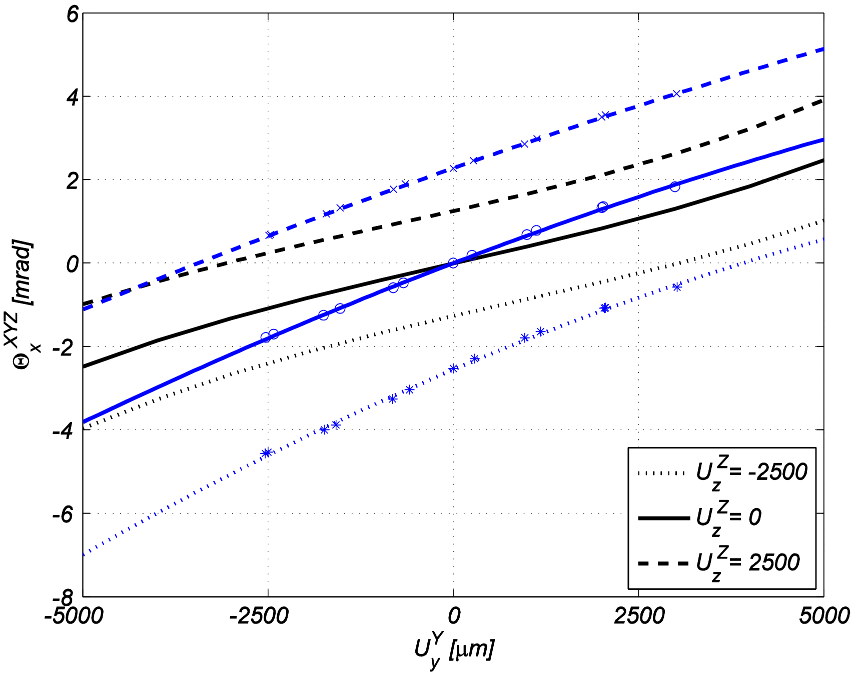

Fig.45 X Direction Rotation of the XYZ Stage

The maximum measured X direction rotation of the XYZ stage is -4.6 *mrad* when U_y^Y is -2536 μm and U_z^Z is -2500 μm. This equates to a maximum X direction rotation of the XYZ stage of -6.98 *mrad* when U_y^Y is -5000 μm and U_z^Z is -5000 μm. Because of design symmetry, the XYZ stage rotation about the Y direction (θ_y^{XYZ}) depends similarly on the X and Z actuation but not as much on the Y actuation. And, the XYZ stage rotation about the Z direction (θ_z^{XYZ}) depends on the X and Y actuation, but not as much on the Z actuation.

Below, I summarize the motion performance of the XYZ flexure mechanism:

i. 10 *mm* motion range in each direction, with the stiffness remaining invariant with actuation along the other two directions.
ii. Lost motion per axis less than 1.7 *mm* over the entire motion range (< 17% of range).
iii. Cross-axis error less than 1.16 *mm* over the entire motion range (< 11.6% of range).
iv. Actuator isolation less than 0.172 *mm* in any given direction over the entire motion range (< 1.72% of range).
v. Parasitic rotations of the XYZ stage less than 6.98 *mrad* over the entire motion range.

Although the experimental data show a greater-than-expected DoF stiffness and a less-than-expected DoC stiffness, the flexure mechanism still demonstrated geometric decoupling between the three axes, large motion range, and relatively small error motions. Discrepancies between the experimental data and the FEA may be due to one or more of the following shortcomings. Although great care was taken in selecting appropriate FEA parameters, the element types may include certain assumptions that limit their prediction of rotations resulting from complex structural loading. Additionally, the mesh density was limited by the available computational power, and could be improved given more time and resources. Considering the experimental setup, data collection was limited by the tolerance of the linear optical encoders to off-axis motions. Encoders with lower resolution, but higher tolerances to off-axis motion, could be used to collect complete data. Also, the load cell used showed a significant amount of drift between tests, limiting its trustworthiness. Finally, the bearing itself has a large, but finite, joint stiffness between PFMs. Relative motion between the ends of the PFMs, especially sliding motion, would result in errors that are very difficult to predict.

As previously discussed, the error motions are expected to be significantly reduced if the actuation force can be applied closer to the center of stiffness. This could be easily done by fabricating a simple adapter to rigidly mount the actuator to the actuation stage, but in a new desired location. The benefit of reduced error motions would greatly outweigh the impact of the added mass.

CHAPTER VI

Application in Nanopositioning

A nanopositioning setup is designed and fabricated to demonstrate the applicability of the proposed XYZ parallel kinematic flexure mechanism to the field of high-performance motion guidance.

6.1 Sensor and Actuator Selection

To attain nanometric quality end point sensing with a high bandwidth, non-contact sensors and actuators must be used. Linear voice-coil actuators are chosen because they provide noncontact direct control of the actuation force and an acceptably high bandwidth. BEI Kimco Magnetics actuators (model LA24-20-000A) are capable of producing up to 40 *N* while tolerating the off-axis motion of 150 μm inherent in the actuation stages of the flexure mechanism design.

The sensing task along each axis can be broken down into two sub-tasks. The long-range translation of the actuation stage is measured using a ground-mounted linear optical encoder. Renishaw encoders (RELM scale, Si-HN-4000 readhead, and SIGNUM interface) are capable of *5 nm* resolution, *80 mm* measurement range, and off-axis tolerance of 250 μm. The relatively short-range translation (FEA prediction of 490μm) between the actuation stage and the XYZ stage is accompanied by large off-axis motions of the XYZ stage from the other two actuators. A capacitive probe rigidly mounted to the actuation stage can measure this translation without being affected by the off-axis motions. Lion Precision capacitive probes (model # C1A) are capable of a 10 *nm* resolution over a *500 µm* range at *15 KHz* bandwidth.

6.2 Sensor and Actuator Mounting Design

Each of the sensors and actuators has specific mounting requirements that must be adapted to the alignment features of the flexure mechanism. Therefore, adapter plates are designed to incorporate these specific mounting features while still retaining the features necessary to accurately and repeatedly mount to the flexure mechanism, as shown in Fig.46. Additionally, simple mounts are designed for attaching the actuators and encoder readheads to the ground.

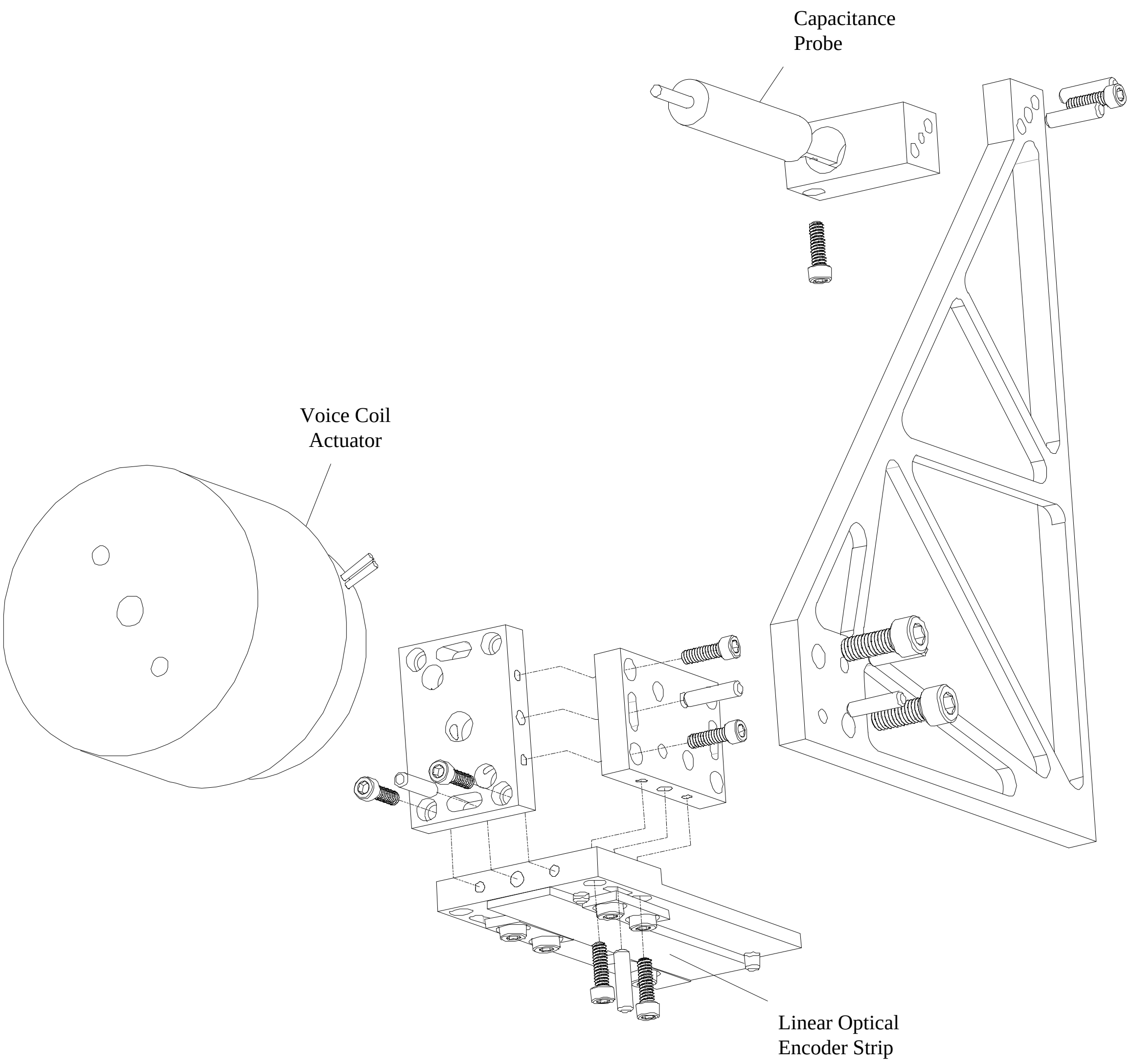

Fig.46 XYZ Nanopositioner Sensor and Actuator Mounts

Mounting the capacitance probes presents a large problem because of their large distance away from the actuation stages. Actuation bandwidth is of great importance to nanopositioning, and therefore mass must be minimized while maintaining sufficient rigidity and maximizing the first fundamental frequency. I designed a truss structure with a first fundamental frequency greater than 20 *Hz* with a maximum stiffness along the capacitance probe axis. The structure was modified based on both dynamic and static FEA results. Fig.47 shows the displacement of the structure under the three directions of gravitational loading.

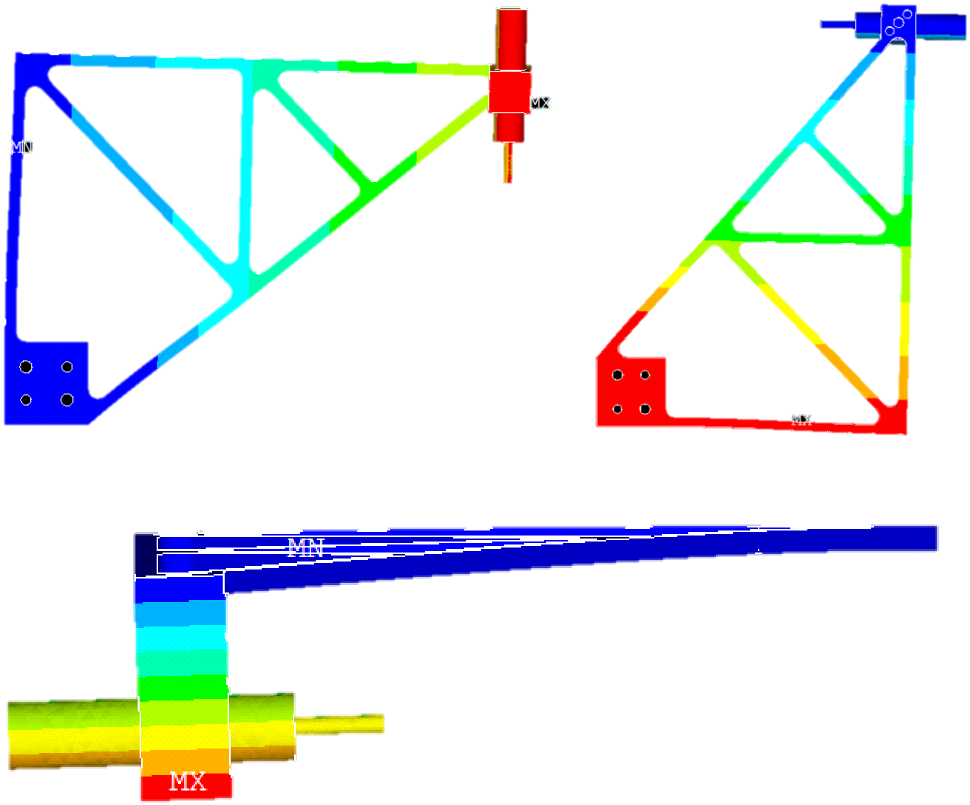

Fig.47 Capacitance Probe Truss FEA Gravitational Loading

6.3 Fabrication

Overall, the entire nanopositioning setup contains a ground plate, two actuator ground mounts, three encoder readhead ground mounts, one flexure mechanism ground mount, and three sets of mounts to attach the sensors and actuators to the flexure mechanism. The ground plate and mounts are designed with standard raw material sizes, and require almost no finish milling. The ground plate is drilled, reamed, and counter-bored after setting the zero point once to ensure proper placement of the mounts. The mounts are also drilled and reamed. The flexure mechanism sensor and actuator mounts require more finish milling work before the holes are created. However, all of the parts have block shapes with perpendicular edges, greatly simplifying machine setup.

The only part not fabricated on the mill is the capacitance probe truss. Due to the complex geometry, the trusses are cut using the water jet. Subsequently, the trusses are mounted on the mill to face the inner trusses, and to drill and ream the mounting holes. The final assemblies are shown in Fig.48 and Fig.49 below.

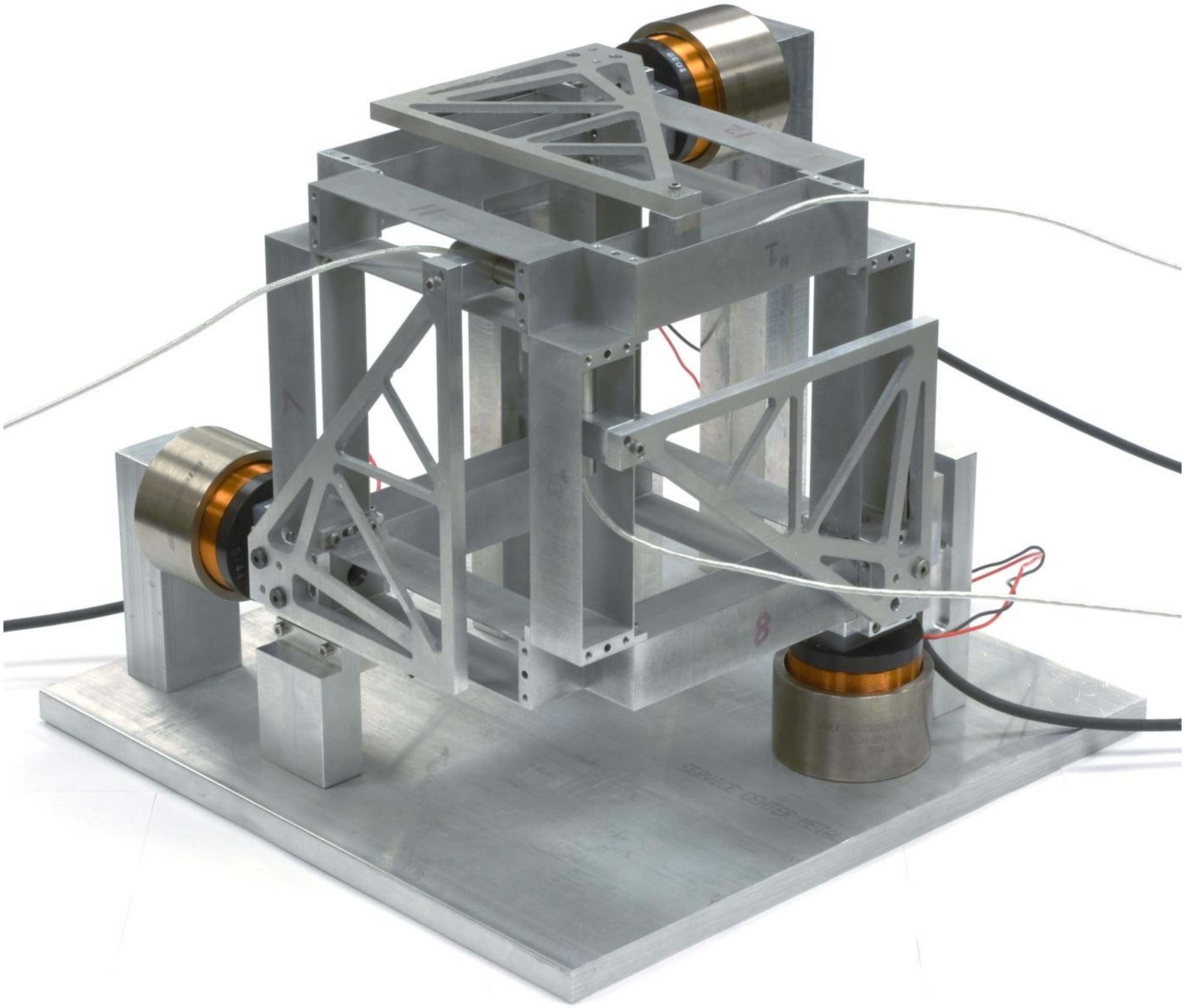

Fig.48 XYZ Nanopositioner Setup (Front View)

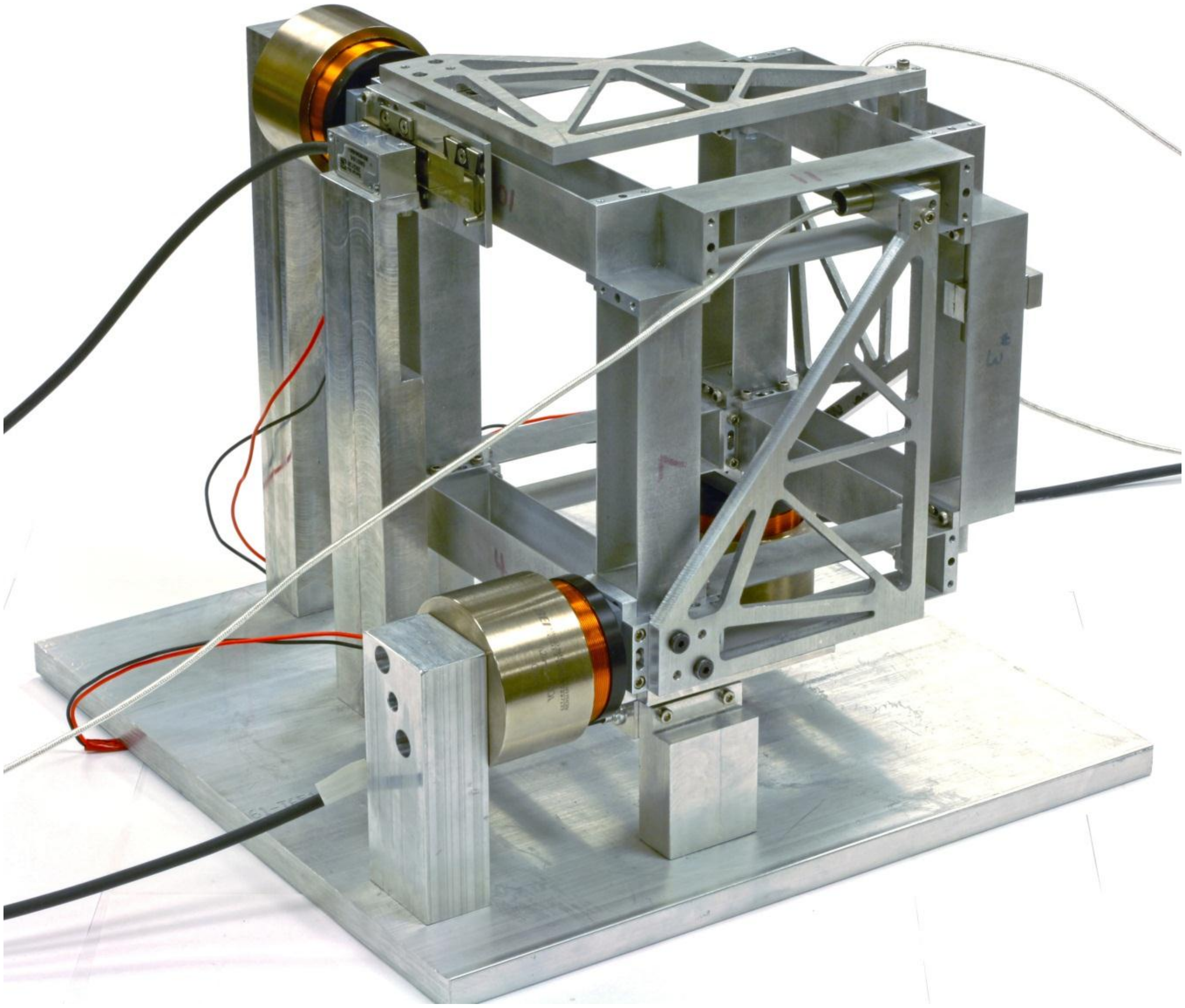

Fig.49 XYZ Nanopositioner Setup (Side View)

Although the nanopositioning setup does not yet provide true nanopositioning capabilities, it does demonstrate the applicability of the XYZ flexure mechanism for such use. After development of a controller, this setup should be capable of providing end-point motion control on the order of nanometers.

APPENDIX A

PFM Fabrication Procedure

Several manufacturing methods were considered for fabricating the PFMs, including CNC milling, water jet cutting, and wire electric discharge machining (EDM). While CNC milling machines can produce linear tolerances better than 0.0002 *in* with very good surface finish, the shearing process of an end mill requires side loads to keep the bit pressed against the material. These side loads would deflect the thin flexures, producing inconsistent flexure thicknesses. Water jet cutting, on the other hand, uses a stream of high pressure water-aggregate mix to blast through the material. This process does not add any thermal stresses to the material, which is important in flexure production. Based on the speed and settings of the machine, linear tolerances better than 0.001 *in* can be achieved. However, the water stream expands as it cuts through the material, creating a slight taper across the width of each beam. Finally, wire EDM cuts through material using a thin metal wire that acts as an electrode when a charge is applied. An arc is formed between the wire and the raw material, eroding the material at the point of the arc. Like the water jet cutter, the wire EDM does not apply side loads to the material. However, the wire EDM can achieve much higher tolerances around 0.00015 *in*. Wire EDM is the best choice for fabricating the delicate and tolerance-sensitive PFMs.

Ultimately, the decision to use wire EDM was made based on the tolerance specifications shown in the engineering drawing in Fig.50. The flexure thickness has the greatest impact on bearing performance; therefore, it has a tolerance of ±0.0005 *in*. The relative alignment of the PFMs is also critical; therefore, the dowel features have a positioning tolerance of ±0.0005 *in*. The tolerances on remaining features, such as screw holes, are not as important.

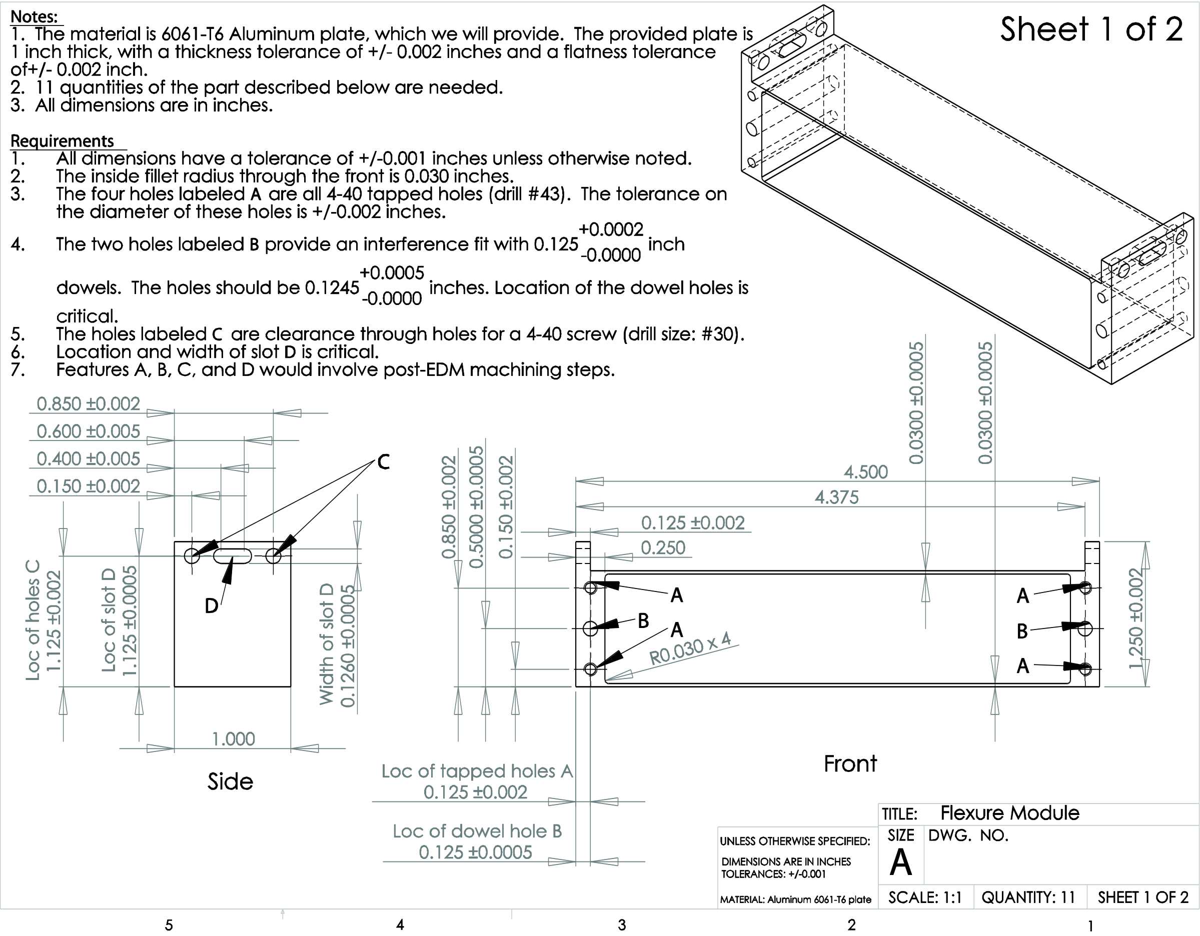

Notes:
1. The material is 6061-T6 Aluminum plate, which we will provide. The provided plate is 1 inch thick, with a thickness tolerance of +/- 0.002 inches and a flatness tolerance of+/- 0.002 inch.
2. 11 quantities of the part described below are needed.
3. All dimensions are in inches.

Requirements
1. All dimensions have a tolerance of +/-0.001 inches unless otherwise noted.
2. The inside fillet radius through the front is 0.030 inches.
3. The four holes labeled **A** are all 4-40 tapped holes (drill #43). The tolerance on the diameter of these holes is +/-0.002 inches.
4. The two holes labeled **B** provide an interference fit with $0.125^{+0.0002}_{-0.0000}$ inch dowels. The holes should be $0.1245^{+0.0005}_{-0.0000}$ inches. Location of the dowel holes is critical.
5. The holes labeled **C** are clearance through holes for a 4-40 screw (drill size: #30).
6. Location and width of slot **D** is critical.
7. Features A, B, C, and D would involve post-EDM machining steps.

Fig.50 PFM Engineering Drawing

Because not all of the features are on one plane, manufacturing was a multi-step process. First, the outer dimensions were cut by EDM from a 1 *in* thick, precision ground plate of 6061 Aluminum. Next, a jig was created to accurately mount the PFMs in the machine so that the inner portion could be removed. Once the flexures were cut, the parts were then mounted to a CNC mill for precision drilling and reaming of the end plate alignment features. The end result is shown in Fig.51.

Fig.51 Rendered PFM

APPENDIX B

Experimental Procedure

Before All Tests

1. Mount Encoders
    a. Strips
        i. Align with the two dowels.
        ii. Attach datum clamps using metal spacer, then tighten.
        iii. Attach tension clamp with spacer.
        iv. Make sure that the strip is against both dowels and that the clamps do not touch the sides of the strip.
    b. Readhead
        i. Attach to mounts using two M3 screws.
        ii. Align so that the indicator turns green and tighten the screws. You may need to use shims to get good alignment. This does not need to be perfect because the encoders will be fine-tuned once the actuators are mounted.
2. Mount Load Cell
    a. Screw the load cell into the X Stage decoupler. Make sure that it sits flush.
3. Mount Actuators
    a. X Stage DC Mike
        i. Screw the load cell adapter into the end of the DC Mike.
        ii. Screw the DC Mike into the load cell until it is connected. Do not tighten too much because the load cell is delicate.
        iii. Make sure the DC Mike is about halfway in its range. If it not, carefully apply voltage to get it there.
        iv. Tighten the DC Mike into the X actuator mount.
        v. To make sure the X stage is at its neutral position:
            1. Run the DSpace program to view the output of the cap probes.
            2. Move the X actuator (by commanding small positions) until the cap probe reading show a minimum displacement. This is the X zero position.
    b. Y and Z Stage DC Mikes (or dummy actuators)
        i. Mount the actuators to the decoupler adapters.
        ii. If using DC Mikes, adjust the position until it is in the middle of its range.
        iii. To make sure the Y and Z stages are in their neutral positions
            1. Hold a gage block (preferably 4 inches long) against the appropriate flexure.

                2. Adjust the actuator until no gap can be seen between the gage block and the flexure. This is the zero position.

Sensor Setup 1 (Cap probes in Z Axis of X Stage)

This setup measures the actuation force and Z translation of the X stage against X actuation for various Y and Z actuations.

4. Mount Cap Probes
    a. Using super glue, carefully (and quickly) attach the ground aluminum plate to the side of the X Stage. First clean the two surfaces with acetone to remove any residual glue. Use only two drops of glue on the X stage, making sure to avoid the dowel and screw holes. Hold the plate firmly against the stage, checking that it is flush.
    b. Tighten the mount to the ground.
    c. Insert the three C1-A cap probes. Facing the negative Z direction, the top left is CP1, the top right is CP2, and the bottom left is CP3.
    d. Make sure all three probes are in “high-sensitivity” mode. Adjust each probe until the indicator LED reads one unit above “near”, and then tighten the screws. This is because the stage is expected to only move further away with all inputs.
5. Run the tests
    a. For each test, Y and Z are held at a fixed position while X is cycled using a controller from 0 to +3mm to 0 to -3mm to 0 in 1mm increments. Each transition is a 1 second ramp, and each position is held constant for 10 seconds. The total test time is 145 seconds.
    b. For the first test (Y = 0, Z = 0)
        i. Align the encoders
            1. Connect the encoders to the PC using the USB output.
            2. Run the Signum Software to view the signal strength and pitch of the readhead.
            3. Adjust each readhead until the signal is close to 100% and the pitch is level. Note: the signal can read 100% even if the pitch is not level. This can cause bad results as the encoders will lose signal more rapidly to small changes. Always make sure that the pitch is level.
        ii. Zero the load cell.
        iii. Zero the cap probes (if desired).
        iv. Run the test and save the data.
    c. To switch to another Y, Z location

        i. It is important to run all tests sequentially and record all data while moving. This is because the encoder outputs are zeroed at the beginning of each test.
        ii. Run the DSpace program with the X command sequence turned off.
        iii. Adjust the Y, Z locations to the next step (e.g. move Z from 0mm to +2.5mm).
        iv. Adjust the X location manually to find its natural zero (this can shift between tests because the controller doesn't always return exactly to zero).
        v. Wait for the outputs to settle for about 10 seconds.
        vi. Stop the program and save.
    d. Run the next test
        i. Align the encoders
            1. Connect the encoders to the PC using the USB output.
            2. Run the Signum Software to view the signal strength and pitch of the readhead.
            3. Adjust each readhead until the signal is close to 100% and the pitch is level. Note: the signal can read 100% even if the pitch is not level. This can cause bad results as the encoders will lose signal more rapidly to small changes. Always make sure that the pitch is level.
        ii. Do NOT zero the load cell or cap probes.
        iii. Run the test with the X command sequence turned on and save the data, keeping an eye on the encoder signal strength.

Sensor Setup 2 (Cap probes in Y Axis of X Stage)

This setup measures the Y translation of the X stage against Y actuation for various Z actuations.

1. Mount the cap probes
    a. Tighten the mount to the ground.
    b. Insert two C1-A cap probes. Facing the negative Z direction, the left is CP1 and the right is CP2.
    c. One additional C1-A cap probe can be mounted along the Z axis of the X stage to measure the zero location of the X stage.
    d. Make sure all three probes are in "high-sensitivity" mode. Adjust each probe until the indicator LED is in the middle, and then tighten the screws.
2. Run the tests
    a. For each test, X is held at 0, Y is fixed, and Z is cycled either manually or using a controller from 0 to +3mm to 0 to -3mm to 0 in 1mm increments.

Each transition is a 1 second ramp, and each position is held constant for 10 seconds. The total test time is 145 seconds.

b. For the first test (X = 0, Y = 0)
    i. Align the encoders
        1. Connect the encoders to the PC using the USB output.
        2. Run the Signum Software to view the signal strength and pitch of the readhead.
        3. Adjust each readhead until the signal is close to 100% and the pitch is level. Note: the signal can read 100% even if the pitch is not level. This can cause bad results as the encoders will lose signal more rapidly to small changes. Always make sure that the pitch is level.
    ii. Zero the load cell.
    iii. Zero the cap probes (if desired).
    iv. Run the test and save the data.

c. To switch to another Y location
    i. It is important to run all tests sequentially and record all data while moving. This is because the encoder outputs are zeroed at the beginning of each test.
    ii. Run the DSpace program with the X command sequence turned off.
    iii. Adjust the Y location to the next step (e.g. move Y from 0mm to +2.5mm).
    iv. Wait for the outputs to settle for about 10 seconds.
    v. Stop the program and save.

d. Run the next test
    i. Align the encoders
        1. Connect the encoders to the PC using the USB output.
        2. Run the Signum Software to view the signal strength and pitch of the readhead.
        3. Adjust each readhead until the signal is close to 100% and the pitch is level. Note: the signal can read 100% even if the pitch is not level. This can cause bad results as the encoders will lose signal more rapidly to small changes. Always make sure that the pitch is level.
    ii. Do NOT zero the load cell or cap probes.
    iii. Run the test with the Z command sequence turned on and save the data, keeping an eye on the encoder signal strength.

Sensor Setup 3 (Cap probes in Z Axis of XYZ Stage)

This setup measures the X rotation of the XYZ stage against Y actuation for various Z actuations.

1. Mount the cap probes
    a. Using super glue, carefully (and quickly) attach the ground aluminum plate to the XY plane of the XYZ Stage. First clean the two surfaces with acetone to remove any residual glue. Use only two drops of glue on the XYZ stage, making sure to avoid the dowel and screw holes. Hold the plate firmly against the stage, checking that it is flush.
    b. Tighten the mount to the ground.
    c. Insert the three C1-A cap probes. Facing the negative Z direction, the top left is CP1, the top right is CP2, and the bottom right is CP3.
    d. Make sure all three probes are in "low-sensitivity" mode. Adjust each probe until the indicator LED is in the middle, and then tighten the screws.
2. Run the tests
    a. For each test, X is held at 0, Z is fixed, and Y is cycled either manually or using a controller from 0 to +3mm to 0 to -3mm to 0 in 1mm increments. Each transition is a 1 second ramp, and each position is held constant for 10 seconds. The total test time is 145 seconds.
    b. For the first test (X = 0, Z = 0)
        i. Align the encoders
            1. Connect the encoders to the PC using the USB output.
            2. Run the Signum Software to view the signal strength and pitch of the readhead.
            3. Adjust each readhead until the signal is close to 100% and the pitch is level. Note: the signal can read 100% even if the pitch is not level. This can cause bad results as the encoders will lose signal more rapidly to small changes. Always make sure that the pitch is level.
        ii. Zero the load cell.
        iii. Zero the cap probes (if desired).
        iv. Run the test and save the data.
    c. To switch to another Y location
        i. It is important to run all tests sequentially and record all data while moving. This is because the encoder outputs are zeroed at the beginning of each test.
        ii. Run the DSpace program with the Y command sequence turned off.

        iii. Adjust the Y location to the next step (e.g. move Z from 0mm to +2.5mm).
        iv. Wait for the outputs to settle for about 10 seconds.
        v. Stop the program and save.
    d. Run the next test
        i. Align the encoders
            1. Connect the encoders to the PC using the USB output.
            2. Run the Signum Software to view the signal strength and pitch of the readhead.
            3. Adjust each readhead until the signal is close to 100% and the pitch is level. Note: the signal can read 100% even if the pitch is not level. This can cause bad results as the encoders will lose signal more rapidly to small changes. Always make sure that the pitch is level.
        ii. Do NOT zero the load cell or cap probes.
        iii. Run the test with the Y command sequence turned on and save the data, keeping an eye on the encoder signal strength.

Sensor Setup 4 (Cap probes in Z Axis of XYZ Stage)

This setup measures the X direction lost motion against X and Y actuations with Z fixed at 0.

1. Mount the cap probes
    a. Using super glue, carefully (and quickly) attach the ground aluminum plate to the YZ plane of the XYZ Stage. First clean the two surfaces with acetone to remove any residual glue. Use only two drops of glue on the XYZ stage, making sure to avoid the dowel and screw holes. Hold the plate firmly against the stage, checking that it is flush.
    b. Tighten the mount to the ground.
    c. Insert the three C1-A cap probes. Facing the negative X direction, the top left is CP1, the top right is CP2, and the bottom right is CP3.
    d. Make sure all three probes are in “low-sensitivity” mode. Adjust each probe until the indicator LED is in the middle, and then tighten the screws.
2. Run the tests
    a. For each test, Z is held at 0, and either X or Y is fixed while the other is cycled either manually or using a controller from 0 to +3mm to 0 to -3mm to 0 in 1mm increments. Each transition is a 1 second ramp, and each position is held constant for 10 seconds. The total test time is 145 seconds.
    b. For the first test (Z = 0, Y = 0)
        i. Align the encoders

1. Connect the encoders to the PC using the USB output.
2. Run the Signum Software to view the signal strength and pitch of the readhead.
3. Adjust each readhead until the signal is close to 100% and the pitch is level. Note: the signal can read 100% even if the pitch is not level. This can cause bad results as the encoders will lose signal more rapidly to small changes. Always make sure that the pitch is level.

ii. Zero the load cell.
iii. Zero the cap probes (if desired).
iv. Run the test and save the data.

c. To switch to another Y location

i. It is important to run all tests sequentially and record all data while moving. This is because the encoder outputs are zeroed at the beginning of each test.
ii. Run the DSpace program with the X command sequence turned off.
iii. Adjust the Y location to the next step (e.g. move Z from 0mm to +2.5mm).
iv. Wait for the outputs to settle for about 10 seconds.
v. Stop the program and save.

d. Run the next test

i. Align the encoders

1. Connect the encoders to the PC using the USB output.
2. Run the Signum Software to view the signal strength and pitch of the readhead.
3. Adjust each readhead until the signal is close to 100% and the pitch is level. Note: the signal can read 100% even if the pitch is not level. This can cause bad results as the encoders will lose signal more rapidly to small changes. Always make sure that the pitch is level.

ii. Do NOT zero the load cell or cap probes.
iii. Run the test with the X command sequence turned on and save the data, keeping an eye on the encoder signal strength.

Note: If the encoders become misaligned too much, the output will stray from actual. If the X encoder strays, the test will need to be rerun. As another check, rerun the first test at the end and look for drift in either the load cell or the cap probes. If the drift is significant, all of the tests will need to be rerun.

REFERENCES

[1] Jones, R. V., 1962, "Some uses of elasticity in instrument design," Journal of Scientific Instruments, (39), pp.193-203

[2] Smith, S. T., 2000, *Flexures: Elements of Elastic Mechanisms*, Gordon and Breach Science Publishers

[3] Slocum, A. H., 1992, *Precision Machine Design*, Society of Manufacturing Engineers, Dearborn, MI

[4] Awtar, S., Ustick, J., and Sen, S., 2011, "An XYZ Parallel Kinematic Flexure Mechanism with Geometrically Decoupled Degrees of Freedom," Proc. ASME IDETC/CIE, Washington DC, Paper # 47713

[5] Fischer, F. L., 1981, Symmetrical 3 DOF Compliance Structure, US Patent 4,447,048

[6] Bednorz, J. G., Hollis Jr., R. L., Lanz, M., Pohl, W. D., and Yeack-Scranton, C. E., 1985, Piezoelectric XY Positioner, 4,520,570

[7] Davies, P. A., 2001, Positioning Mechanism, US 6,193,226

[8] Dagalakis, N. G., and Amatucci, E., 2001, "Kinematic Modeling of a 6 Degree of Freedom Tri-Stage Micro-Positioner," Proc. ASPE 16th Annual Meeting, Crystal City VA

[9] Yao, Q., Dong, J., and Ferreira, P. M., 2008, "A novel parallel-kinematics mechanisms for integrated, multi-axis nanopositioning. Part 1. Kinematics and design for fabrication," Precision Engineering, 32(1), pp.7-19

[10] Hicks, T. R., and Atherton, P. D., 1997, *The Nanopositioning Book*, Queensgate Instruments Ltd.

[11] Application Note: Nanopositioning Tools and Techniques for R&D Applications, nPoint Inc.

[12] Jordan, S., and Lula, B., 2005, "Nanopositioning: The Technology and the Options," The 2005 Photonics Handbook

[13] Dai, G., Pohlenz, F., Danzebrink, H.-U., Xu, M., Hasche, K., and Wilkening, G., 2004, "Metrological large range scanning probe microscope," Review of Scientific Instruments, 75(4), pp.962-969

[14] Sinno, A., Ruaux, P., Chassagne, L., Topcu, S., and Alayli, Y., 2007, "Enlarged Atomic Force Microscopy Scanning Scope: Novel Sample-holder Device with Millimeter Range," Review of Scientific Instruments, 78(9), pp.1-7

[15] Wouters, D., and Schubert, U. S., 2004, "Nanolithography and nanochemistry: Probe-related patterning techniques and chemical modification for nanometer-sized devices," Angewandte Chemie International Edition, 43(19), pp.2480–2495

[16] Beeby, S., Tudor, M., and White, N., 2006, "Energy harvesting vibration sources for microsystems applications," Measurement Science and Technology, (12), pp.R175-R195

[17] Mitcheson, P. D., Rao, G. K., and Green, T. C., 2008, "Energy Harvesting From Human and Machine Motion for Wireless Electronic Devices," Proc. IEEE, 96(9), pp.1457-1486

[18] Smith, S. T., and Seugling, R. M., 2006, "Sensor and actuator considerations for precision, small machines," Precision Engineering, 30(3), pp. 245-264

[19] Awtar, S., and Slocum, A. H., 2007, "Constraint-based Design of Parallel Kinematic XY Flexure Mechanisms," ASME Journal of Mechanical Design, 129(8), pp.816-830

[20] Blanding, D. L., 1999, *Exact Constraint: Machine Design Using Kinematic Principles*, ASME Press, New York

[21] Hopkins, J. B., and Culpepper, M. L., 2010, "Synthesis of multi-degree of freedom, parallel flexure system concepts via Freedom and Constraint Topology (FACT) - Part I: Principles," Precision Engineering, 34(2), pp.259-270
[22] Su, H.-J., and Tari, H., 2010, "Realizing orthogonal motions with wire flexures connected in parallel," ASME Journal of Mechanical Design, 132(12)
[23] Awtar, S., Shimotsu, K., and Sen, S., 2010, "Elastic Averaging in Flexure Mechanisms: A Three-Beam Parallelogram Flexure Case Study," Journal of Mechanisms and Robotics, 2(4)
[24] Culpepper, M. L., and Anderson, G., 2004, "Design of a low-cost nano-manipulator which utilizes a monolithic, spatial compliant mechanism," Precision Engineering, 28(4), pp.469-482
[25] Yamakawa, K., Furutani, K., and Mohri, N., 1999, "XYZ-stage for Scanning Probe Microscope by Using Parallel Mechanism," Proc. ASME DETC
[26] Li, Y., and Xu, Q., 2005, "Kinematic Design of a Novel 3-DOF Compliant Parallel Manipulator for Nanomanipulation," Proc. 2005 IEEE/ASME International Conference on Advanced Intelligent Mechatronics, Monterey, CA
[27] Arai, T., Herve, J. M., and Tanikawa, T., 1996, "Development of 3 DOF micro finger," Proc. Intelligent Robots and Systems '96
[28] Xueyen, T., and Chen, I. M., 2006, "A Large-Displacement and Decoupled XYZ Flexure Parallel Mechanism for Micromanipulation," Proc. IEEE International Conference on Automation Science and Engineering
[29] Hao, G., and Kong, X., 2009, "A 3-DOF Translational Compliant Parallel Manipulator Based on Flexure Motion," Proc. ASME IDETC, Paper # 49040
[30] Li, F., Wu, M. C., Choquette, K. D., and Crawford, M. H., 1997, "Self-assembled microactuated XYZ stages for optical scanning and alignment," Proc. TRANSDUCERS '97, Chicago
[31] Ando, Y., 2004, "Development of three-dimensional electrostatic stages for scanning probe microscope," Sensors and Actuators A: Physical, 114(2-3), pp.285-291
[32] Mcneil, A. C., Li, G., and Koury, D. N., 2005, Single Proof Mass 3 Axis MEMS Transducer, US 6,936,492
[33] Xinyu, L., Kim, K., and Sun, Y., 2007, "A MEMS stage for 3-axis nanopositioning," Journal of Micromechanics and Microengineering, 17(9)
[34] Sarkar, N., Geisberger, A., and Ellis, M. D., 2004, Fully Released MEMS XYZ Flexure Stage with Integrated Capacitive Feedback, US Patent 6,806,991
[35] XYZ Flexure Demonstration Video, http://www-personal.umich.edu/~awtar/XYZ%20flexure%20video1.mp4
[36] Awtar, S., Slocum, A. H., and Sevincer, E., 2007, "Characteristics of Beam-based Flexure Modules," ASME Journal of Mechanical Design, 129(6), pp.625-639
[37] Awtar, S., and Parmar, G.., 2010,"Design of a Large Range XY Nanopositioning System", Proc. IDETC/CIE 2010, Montreal, Canada, Paper No. 28185
[38] Awtar, S., 2011, Multiple Degrees of Freedom Motion System, US 8,072,120
[39] Chen, K. S., Trumper, D. L., and Smith, S. T., 2002, "Design and control for an electromagnetically driven X-Y-Θ stage," Precision Engineering, 26(4)
[40] Siddall, G. J., 1987, Flexure Stage Alignment Apparatus, US 4,694,477

[41] Awtar, S., Trutna, T. T., Nielsen, J. M., Abani, R., and Geiger, J. D., 2010, "FlexDex: A Minimally Invasive Surgical Tool with Enhanced Dexterity and Intuitive Actuation," ASME Journal of Medical Devices, 4(3)

[42] Du, E., Cui, H., and Zhu, Z., 2006, "Review of nanomanipulators for nanomanufacturing," International Journal of Nanomanufacturing, 1(1)

[43] Howell, L. L., 2001, *Compliant Mechanisms*, John Wiley & Sons

[44] Awtar, S., Slocum, A.H., and Sevincer E., 2007, "Characteristics of Beam-based Flexure Modules", ASME Journal of Mechanical Design, 129 (6), pp. 625-639

[45] Dai, G., Pohlenz, F., Danzebrink, H.-U., Xu, M., Hasche, K., and Wilkening, G., 2004, "Metrological large range scanning probe microscope," Review of Scientific Instruments, 75(4), pp. 962-969.

[46] Hausotte, T., Jaeger, G., Manske, E., Hofmann, N., and Dorozhovets, N., 2005, "Application of a Positioning and Measuring Machine for Metrological Long-range Scanning Force Microscopy," Proc. SPIE, San Diego, CA, 5878(2), pp. 1-12.

[47] Sinno, A., Ruaux, P., Chassagne, L., Topcu, S., and Alayli, Y., 2007, "Enlarged Atomic Force Microscopy Scanning Scope: Novel Sample-holder Device with Millimeter Range," Review of Scientific Instruments, 78(9), pp. 1-7.

[48] Weckenmann, A., and Hoffmann, J., 2007, "Long Range 3D Scanning Tunneling Microscopy," CIRP Annals - Manufacturing Technology, 56(1), pp. 525-528.

[49] Salaita, K., Wang, Y. H., and Mirkin, C. A., 2007, "Applications of Dip-Pen Nanolithography," Nature Nanotechnology, 2(3), pp. 145-55.

[50] O'brien, W., 2005, "Long-range motion with nanometer precision," Photonics Spectra, 39

[51] Zhu, D., & Beeby, S. (2011). “Chapter 1: Kinetic Energy Harvesting,” *Energy Harvesting Systems: Principles, Modeling and Applications*, pp. 1-14.

[52] Hopkins, J. B., and Culpepper, M. L., 2010, "Synthesis of multi-degree of freedom, parallel flexure system concepts via Freedom and Constraint Topology (FACT) - Part III: Numerations and Type Synthesis of Flexure Mechanisms," Precision Engineering.

[53] Huang Z., and Li Q.C. 2003, “Type synthesis of symmetrical lower-mobility parallel mechanisms using the constraint synthesis method”. *International Journal of Robotics Research*, 22(1): 59-79.

[54] Fang Y.F., and Tsai L.W. 2002, “Structure synthesis of a class of 4-DoF and 5-DoF parallel manipulators with identical limb structures”. *International Journal of Robotics Research*, 21(9): 799-810.